1. Study of Quaternary AlInGaN grown by Metal-Organic Chemical Vapor Deposition on Sapphire Substrate

Study of Quaternary AlInGaN grown by Metal-Organic Chemical Vapor Deposition on Sapphire Substrate

Abstract:

In this report, the growth of AlInGaN by metal organic chemical vapour deposition (MOCVD) and its application for optoelectronic and electronic device were studied. The growth of AlInGaN was optimized as a function of growth temperature. The great difference of material properties were observed between the AlInGaN samples with same composition grown at different temperatures. The material quality of high temperature grown sample is much superior to that of low temperature one. Base on this point, high quality MQWs structure was grown with a strong PL emission at 350 nm. However, the 350 nm LED was failed to be fabricated because of lack of a proper AlGaN template on sapphire substrate. The electronic application of AlInGaN was also studied, which included the properties of Schottky contact to AlInGaN. Finally, high performance AlInGaN based heterojunction field effect transistors (HFETs) in both enhancement mode (E-mode) and depletion mode (D-mode) were demonstrated for the first time, which indicate quaternary AlInGaN is a promising material for high power and high frequency electronics applications.

1. Introduction:

In the past two decades, the great progress has been made for the research of Group III nitride semiconductors in both optoelectronic and electronic applications, which includes the commercialization of both GaN based green, blue and near Ultraviolet (UV) light emitting diodes (LEDs) and 405 nm laser diodes (LD) for next generation DVD system, and also includes the near commercialization for GaN based heterojunction field effect transistor (HFET) in high power and high frequency electronic device applications.

In recent years, quaternary AlInGaN alloy attracted much attention because of the following reasons. The first, in the view of available wide range of direct bandgaps, wurtzite GaN alloyed with AlN and InN may span a wide and continuous spectrum range from UV to

infrared (IR). This makes the quaternary nitride system attractive for optoelectronic device applications. Second, quaternary AlInGaN can provide the maximum possibility for the combined bandgap and lattice constant engineering. Therefore by adjusting the in-plane strain of the quantum wells, the quantum confined stark effect (QCSE) may be expected to be reduced and the improved emission efficiency may be expected. Third, some researchers [1] found that AlInGaN was a promising material for UV emission in comparison with ternary AlGaN. This may be due to the exciton localization effect, which is similar to the effect of Indium in the InGaN system. The final reason is that quaternary may be a promising candidate as a barrier material of GaN based HFETs, which will be discussed in detail at the following session.

The biggest obstacle of realizing high-quality AlInGaN layers is to optimize a proper growth condition because of the difference in typical growth temperature for ternary alloys AlGaN and InGaN. The growth temperature for high-quality AlGaN can be over 1000°C, while InGaN growth must usually occurs at low temperature (700~800°C) because of the weak In-N bond.

The context of this report will be arranged as following: (1) Growth optimization of AlInGaN; (2) Optoelectronics application for quaternary AlInGaN; (3) Electronics application for quaternary AlInGaN

2. Growth optimization for quaternary AlInGaN

As we mentioned above, because of the great difference in growth temperature between AlGaN and InGaN, the incorporation of both Al and In into GaN would be very difficult. Before we started this project, the published temperatures for AlInGaN growth by metal-organic chemical vapor deposition (MOCVD) varied in a large range from 750 to 875°C. However, the quality of the obtained quaternary AlInGaN epilayers in the literature had not reached a satisfying level yet. Thus, careful optimization on the growth condition was very necessary.

In this section, the quaternary AlInGaN alloys were grown on c-plane sapphire substrates at atmospheric pressure by *Nippon Sanso SR2000 MOCVD* system. Trimethylgallium (TMG), trimethylindium (TMI), trimethylaluminum (TMA) and ammonia (NH_3) were used as source materials. Initially, the sapphire substrate was heated up to 1100°C for 10 min in hydrogen ambient to clean the surface. A 30-nm-thick GaN layer was deposited as a buffer layer at 550°C. Then, the substrate was heated up to 1180°C and a 1.3-μm-thick GaN layer was grown on the GaN buffer layer. Finally, the temperature was decreased to low temperature for quaternary AlInGaN alloys growth. Five undoped AlInGaN samples with similar thickness (~90nm) were grown at 780, 820, 860, 900 and 940°C, respectively. For simplicity, hereinafter, they are abbreviated as S_{780}, S_{820}, S_{860}, S_{900} and S_{940}, respectively. These five samples were designed to have same alloy composition (Al: ~9%, In: ~2%) to facilitate comparing the influence of growth temperature, since the properties of AlInGaN also strongly depend on the content of Al and In [2, 3].

The structural properties of these alloys were characterized using x-ray diffraction (XRD). Al and In compositions of quaternary epilayers were estimated using electron probe microanalysis (EPMA) and verified by XRD. Atomic force microscopy (AFM) was utilized to characterize the surface morphology of the samples. The PL measurements were carried out to characterize the optical properties.

2.1 Surface morphology

All the samples were investigated by optical microscopy and showed a specula mirror surface. However, their AFM morphologies exhibit strong dependence on the growth temperature (see Fig.2.1). Compact columns were distributed on the surface of S_{780} (see Fig.2.1) with peak-valley height up to 60nm, which shows a typical morphology of three-dimensional (3D) growth; whereas for S_{860}, S_{900} and S_{940} (see Fig.2.1c-e), clear step-flow could be observed with lower roughness (see Table I), indicating the two-dimensional (2D) growth. Obviously, the transformation of growth mode happened as temperature increased (see Fig.2.1f). The transition stage could be clearly observed in S_{820} (see Fig.2.1b), in which

coalescence growth was confirmed by the observation of some remained un-coalesced grooves. The temperature dependent morphology can be explained in terms of the increased adatoms mobility with temperature on the growing surface. The improvement of surface

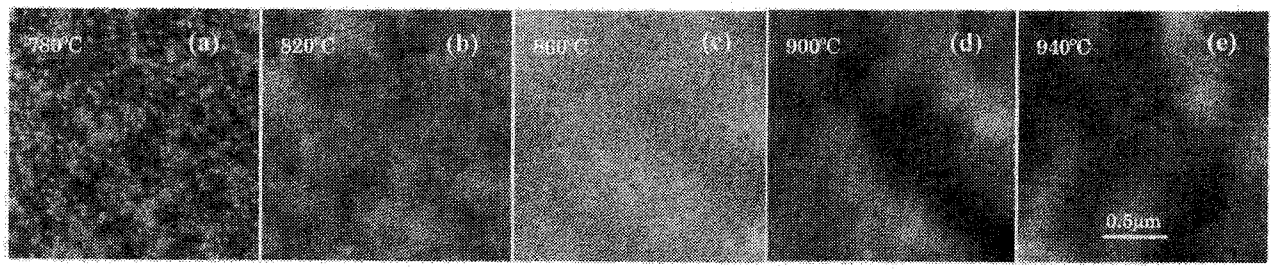

Fig.2.1. AFM picture of five $Al_{0.09}In_{0.02}GaN$ grown at different temperatures.

morphology with temperature is also supported by the observation of pits in S_{860}, S_{900} and S_{940} (see Fig.2.1c-e), in which the depth of pits is notably decreased and pits are hardly observed in S_{900} and S_{940}. The pits in forms of V-defects are always observed in InGaN system [4,5] as an extension of thread dislocation in the underlying GaN layer. A recent research[6] proposed that one route for V-defect formation is the result of a reduced growth temperature.

Table I. The properties of the five AlInGaN samples grown at different temperature.

Sample		**S_{780}**	**S_{820}**	**S_{860}**	**S_{900}**	**S_{940}**
Growth	Temperature (℃)	780	820	860	900	940
AFM	RMS (*nm*)	9.3	0.79	0.62	0.43	0.34
(2 x 2	V-P (*nm*)	60	9.3	12.5	3.2	2.7
XRD	FWHM (*004*) *arcsec*	338	364	290	262	258
	Mismatch $\Delta C/C_0$ (%)	-0.35	-0.32	-0.30	-0.33	-0.35
PL @ RT	FWHM (*meV*)	N/A	71	57	48.8	47.1
	Intensity (*a.u.*)	N/A	4.1	45	93	100
@	FWHM (*meV*)	N/A	74	36	18.7	18.1
Simulation	*E(0)* (*eV*)	-	3.716	3.681	3.669	3.658
Parameters	α (*meV/K*)	-	1.423	1.08	0.97	0.96
	β (*K*)	-	860	860	860	860
	σ (*meV*)	-	29.1	15.3	9	8.4

2.2 Structural properties

The structural properties of AlInGaN were investigated by XRD with *Philips Expert*

MRD system. The results obtained from asymmetrical reciprocal lattice mapping indicated the AlInGaN epilayers were all coherently grown on the thick GaN layers. The the full-width at half-maximum (FWHM) of X-ray rocking curve and out-of-plane lattice mismatches for each sample are listed in the Table I, which indicate the high crystalline quality of high-temperature grown sample. This result is consistent with the observation from AFM.

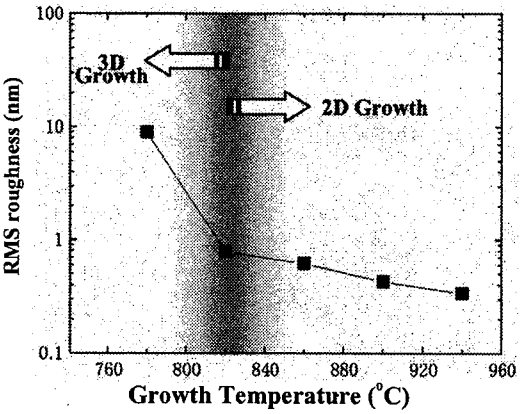

Fig.2.1(f) The plot of AFM roughness (root mean square) of the samples as a function of growth

2.3 Optical properties

The improved quality with growth temperature was also observed from PL measurements that were carried out with He-Cd laser excitation (325 nm, 11 mW) at both room temperature (RT) and 77K, respectively. The normalized spectra were shown in Fig.2.2, in which the spectra of S_{780} were excluded, since no band gap peak could be observed at both RT and 77K except for a broad deep level emission at 77K, which indicates poor optical quality of this sample. Unlike S_{780}, a clear band edge emission was observed at longer wavelength (~370nm) for another 780°C-grown sample with larger In content[7]. We attribute the difference to the In incorporation induced localization effect, since

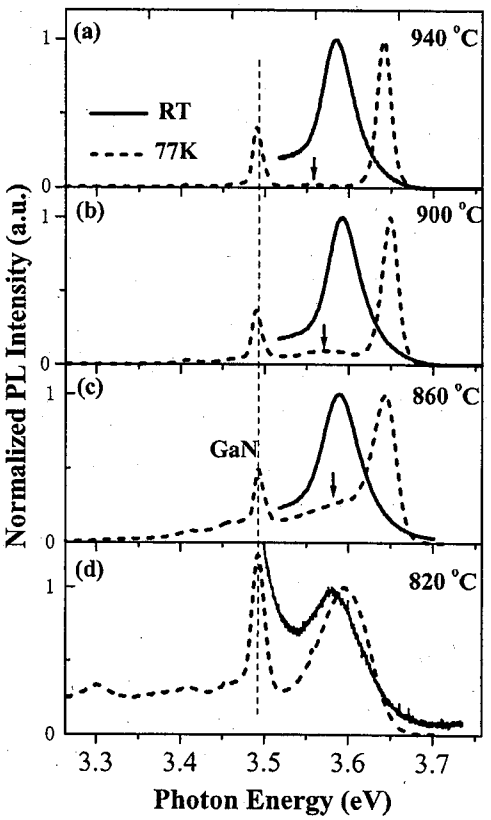

Fig. 2.2 Normalized PL spectra of Sample (a) S940, (b) S900, (c) S860 and (d) S820;

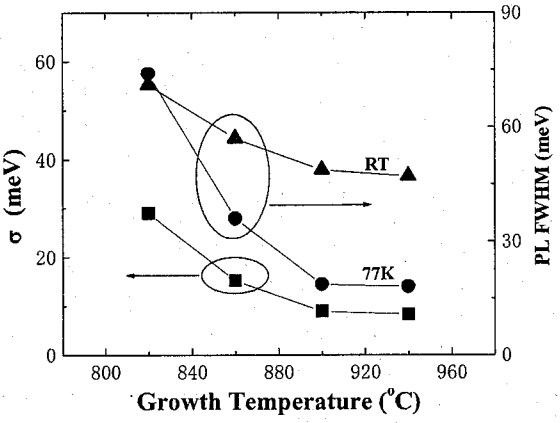

Fig.2.3 FWHM of PL spectra and fitted σ value in Equation (1) as a function of growth temperature.

the optical properties of AlInGaN can be notably improved by increasing indium content[2, 3]. That is the reason why we employed AlInGaN samples with similar alloy compositions for comparison in this section. As shown in Fig.2.2, the four samples all have a clear band edge peak around 346nm at RT (shown with solid line). The peak of underlying GaN layer (located at low energy side of quaternary peak) was not shown to keep the clarity of the figure. Figure 2.3 shows the plot of FWHM values of above samples as a function of growth temperature, in which S_{940} emits with a narrowest peak at both RT (47meV) and 77K (18meV), respectively, indicating the higher optical quality. Such high quality is also supported by the room-temperature PL intensity of S_{940} (see Table I) which is near two orders higher than that of S_{820}. In addition, the observation and suppression of a broad peak labeled with arrows in Fig.2.2 is another supporting evidence. Such peak with a long tail could be observed in a wide temperature range from 60 to 200K. We tentatively assign it to the defects (or impurities) related emission and will discuss it in detail elsewhere. Obviously, this peak can hardly be observed in S_{940} and enhanced notably in the lower-temperature-grown samples, which indicates some defects (or impurities) have been removed at high growth temperature.

It is worth to mention that the four samples exhibit different blue-shift behaviors at 77K (see Fig.2.2) and the blue-shift values varied from 20 to 61meV. We ever claimed [7] that such abnormal behavior was due to the potential minima fluctuation caused by alloy compositional inhomogeneity. In order to gain further insight into the recombination mechanisms, the temperature dependent PL measurements were performed with a helium closed-circuit refrigerator at temperatures ranging from 42 to 300K. Figure 2.4 gives the plot of emission energy as a function of temperature, in which the four samples all exhibit red shift

as the temperature decreasing. This is so-called "S-shaped" temperature dependence behavior (localization effect), which consists of a blue-red-blue-shift as decreasing the temperature. This behavior has been observed in many alloy systems including InGaN[8], AlGaN[9, 10] and AlInGaN [11,12], which can be explained in terms of the localization of carrier or exciton in potential minima (caused by alloy compositional fluctuation) at low temperature and de-localization as increasing the temperature. For S_{900} and S_{940}, the last blue-shift region was not observed, which we believe is due to the limitation of the minimum temperature (42K).

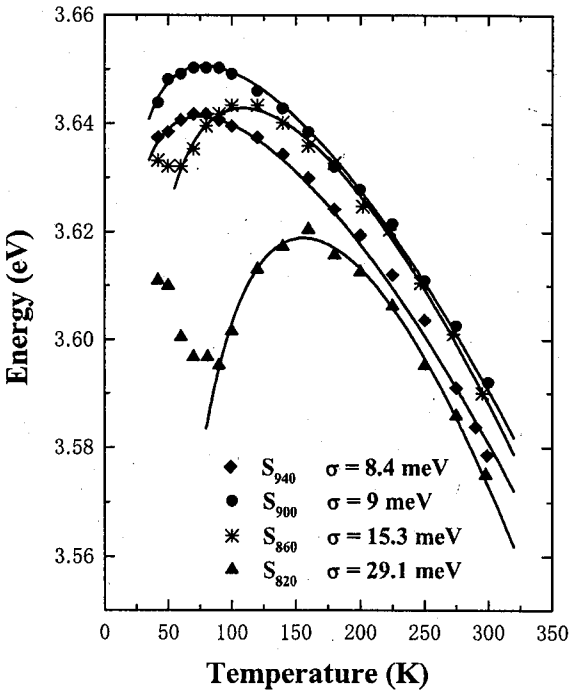

Fig.2.4 Temperature dependence of PL emission energies of the studied samples. The solid curves represent the fits to the experimental data using Equation (2.1).

According to the band tail model, the temperature dependent emission energy curve could be fitted by the following expression[13].

$$E(T) = E(0) - \frac{\alpha T^2}{T+\beta} - \frac{\sigma^2}{K_B T} \qquad (2.1)$$

The first two terms is so-called Varshni's temperature dependence, in which $E(0)$ describes the energy gap at zero absolute temperature; α and β are known as Varshni parameters. The third term was used to describe the localization effect, in which K_B is Bolzmann's constant and σ is called standard deviation of potential fluctuation[10] and indicates the degree of localization effect. Namely, the larger σ value, the stronger localization effect. The solid lines in Fig.2.4 are fitted curves for each sample and the fitted parameters are also given in Table I. The fitted σ values are 29.1, 15.3, 9 and 8.4meV for S_{820}, S_{860}, S_{900} and S_{940}, respectively and they are also plotted as a function of growth temperature in Fig.2.3. The data implies that, for

the same alloy composition AlInGaN, lower growth temperature will result in stronger localization effect (alloy compositional fluctuation), which can be explained in terms of the shorter diffusion length of adatoms at lower growth temperature. The stronger alloy compositional fluctuation is also supported by the larger PL FWHM value of lower-temperature-grown AlInGaN (see Fig.2.3).

It is well known that the localization effect in both InGaN[8] and AlInGaN[3, 12] system is always accompanied with the enhancement of optical emission. This seems to contradict with our case that the PL intensity enhanced with the degradation of localization effect. We assign the contradiction to the different origin of the localization effect in our samples. We think the strong localization effect in S_{820} is mainly attributed to Al-related alloy inhomogeneity, not indium, since the optimum growth temperature for AlGaN is always larger than 1000°C and the optical emission enhancement was never found in AlGaN system even with strong localization effect[9]. Thus we believe the improper Al incorporation at low growth temperature results in poor crystalline quality and strong localization effect, the decrease of σ value in Fig.2.3 is indicative of the improvement of the Al-incorporation quality as increasing growth temperature.

The crystalline quality improvement with growth temperature was further confirmed by the investigation of integrated PL intensity as a function of temperature (see Fig.2.5). The integrated intensity of each sample is normalized by its integrated intensity obtained at 42K. All the samples exhibit the degradation of intensity with the increased temperature. This is well known as thermal quenching, which caused by the thermal activation of non-radiative recombination traps. The degradation of S_{940} shows near 2 orders less than that of

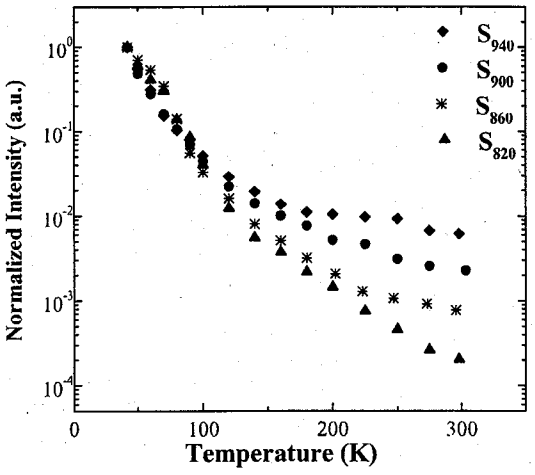

Fig.2.5 Temperature dependence of the normalized integrated PL intensities of the studied samples.

S_{820}, indicating higher quantum efficiency of S_{940}. This implies the non-radiative traps had been significantly reduced at high growth temperature, which may be due to the improvement of Al incorporation.

Based on above-obtained results, we strongly propose high temperature growth (≥ 900°C) for AlInGaN, especially for those with high Al contents. The determination of optimum temperature should be compromised by considering indium incorporation. Although the In incorporation efficiency will decrease with the increase of growth temperature, proper decrease on the indium content is acceptable because a few percent (2~5%) indium incorporation was thought to be sufficiently effective for UV application[3]. On the other hand, the enhancement of indium incorporation at high temperature is possible by means of increasing the growth rate and V/III ratio[14].

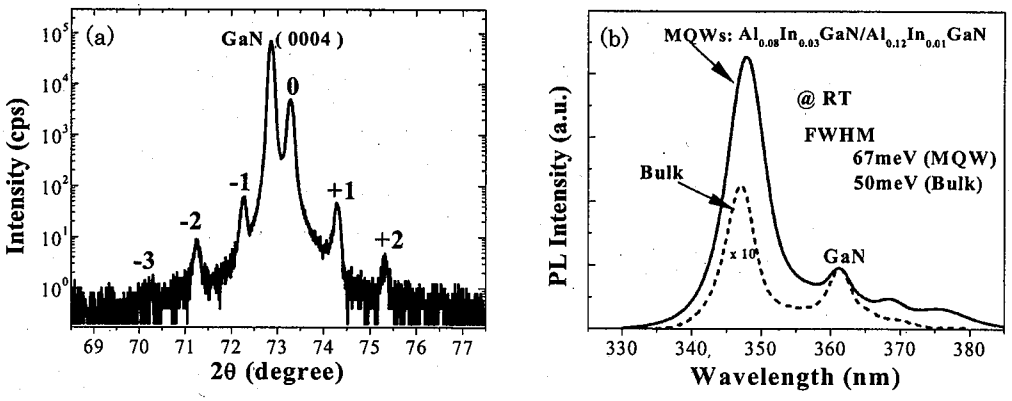

Fig.3.1(a).XRD (0004) plane 2 scan of 10 periods AlInGaN/GaInGaN MQWs grown at 900C, (b). Room temperature PL spectrum of the MQWs (solid line), in which PL spectrum of bulk material was also shown (dash line).

3. Optoelectronics application for quaternary AlInGaN

Basing on the abovementioned research, 10 periods $Al_{0.08}In_{0.03}Ga_{0.89}N/Al_{0.12}In_{0.01}Ga_{0.87}N$ Multiple Quantum Wells (MQWs) structure had been studied. The growth temperature is 900°C. The lattice constant of well quaternary material (Al:8%, In:3%) is similar to that of the underlying GaN and the bandgap energy difference between barrier and well layer is about 150meV. As shown in Fig.3.1, clear multiple satellite peaks in (0004) XRD 2θ~ω scan and a strong RT PL emission at 348nm with very narrow FWHM value of 67meV (6.5nm) are

obtained, indicating high crystalline quality and smooth interfaces in MQWs region. To the best of our knowledge, this is the smallest PL FWHM value obtained from AlInGaN/AlInGaN MQW in the open literature.

Then a LED structure was grown (Fig.3.2a), in which the MQW is same with abovementioned structure. However, the surface of the wafer is full of cracks (see Fig.3.2b). We believe this is due to the large lattice mismatch between the cladding $Al_{0.26}GaN$ layer and GaN template. The best resolution for this problem is to replace the GaN template with AlGaN template, because this can reduce the large strain between the template and cladding layer. However, growth of thick (>1μm) AlGaN on sapphire or silicon substrate is a great challenge for the researchers. Till now, only few group has succeeded in growth of high Al (>50%) content AlGaN template on sapphire substrate. This subject is too large to be solved in current project.

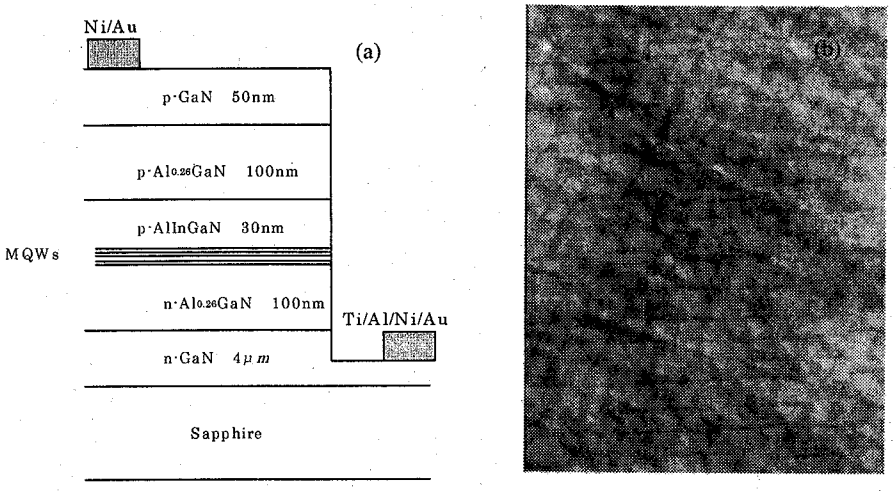

Fig. 3.2 Schematic structure of AlInGaN LED (a) and its surface microscopic picture (b)

4. Electronics application for quaternary AlInGaN

4.1 Introduction

Since the first demonstration of an AlGaN/GaN HFET[15], impressive progress has been made in the field of high-power and high-frequency electronic applications[16]. The high performance of GaN-based HFETs is primarily due to the existence of a high mobility

two-dimensional electron gas (2DEG) at the AlGaN/GaN interface, which is created by a large conduction band offset, and by the strong piezoelectric and spontaneous polarization effects in the heterostructure[17]. Further improvements in HFET performance can be expected if the Al mole fraction of AlGaN barrier layer is increased. However, with this further increase of the Al mole fraction, the increasing lattice mismatch between AlGaN and GaN will decrease the critical thickness for the strained AlGaN barrier, resulting in the generation of misfit dislocations and cracks. To solve the problem, quaternary AlInGaN was proposed[18,19] to replace AlGaN as the barrier material because of following two advantages: First, use of a quaternary allows the independent adjustment of the bandgap and lattice constant, so that the built-in strain can be controlled below the critical. Second, larger polarization may be expected in a quaternary AlInGaN barrier with significant Al mole fraction mainly due to an increase in spontaneous polarization. It has been theoretically[20] predicted that the spontaneous polarization is as large as the piezoelectric polarization in

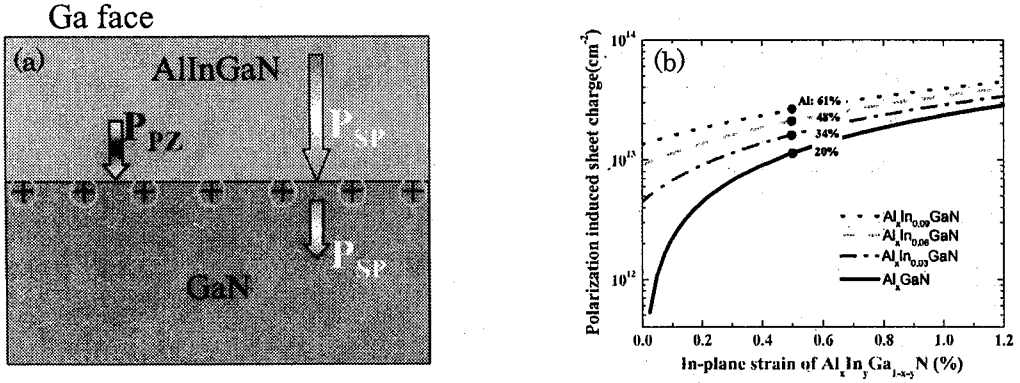

Fig.4.1-1 (a) Schematic structure of AlInGaN/GaN HFET structure. (b) Theoretical calculation of the relation between the in-plane strain of AlInGaN and the polarization induced sheet charge density.

wurtzite group-III nitrides increasing from GaN over InN to AlN. Figure 4.1-1 shows mechanism of the occurrence in polarization-induced sheet charge (PISC) and the theoretical simulation about the relation between the PISC density at the heterojunction interface and the in-plane strain of the hetero-epilayer (AlInGaN). From the figure we can understand that much more PISC density can be available in AlInGaN structure than in AlGaN if we keep the in-plane strain as a constant for both cases. In this section, the properties of Schottky contact

properties on AlInGaN were examined initially, since Schottky contact issue is the key point in the HFET. A large barrier height leads to smaller leakage current and thus improves the noise level and the high voltage performance of the device. Then, the novel AlInGaN HFETs were fabricated on sapphire substrate and some further efforts had been engaged in the research about normally-off operation.

4.2 Schottky contact to quaternary AlInGaN

The Schottky barrier diodes (SBDs) properties were examined on a series of thick undoped AlInGaN with different Al content grown by MOCVD. After the growth of 1.3 μm of undoped GaN on c-plane sapphire substrate, about 400 nm thick AlInGaN was deposited at 900°C. The EPMA measurements revealed that the Al mole fraction of the 4 samples were approximately 7, 9.5, 13.5 and 17%, respectively, and the In mole fraction was about 2%. These four heterostructure samples will be referred to as S1, S2, S3 and S4, respectively, with increasing Al mole fraction. In the following parts, we will discuss the properties of S1 first, since the lattice of AlInGaN epilayer in S1 is lattice matched with GaN, the Al dependent properties will be discussed later.

4.2.1 Near-ideal Schottky contact on AlInGaN epilayer lattice-matched with GaN

From PL measurement, a strong band edge emission at 355nm was observed (see Fig.4.2.1-1) from S1 with narrow full-width at half-maximum value of 52 meV, implying the high crystalline quality. The shoulder peak at longer wavelength originated from underlying GaN layer. Lattice matching in AlInGaN/GaN heterostructure was confirmed by the observation of the overlapping of AlInGaN and GaN peaks in X-ray diffraction (XRD) spectrum (see the inset of Fig.4.2.1-1.). Thus,

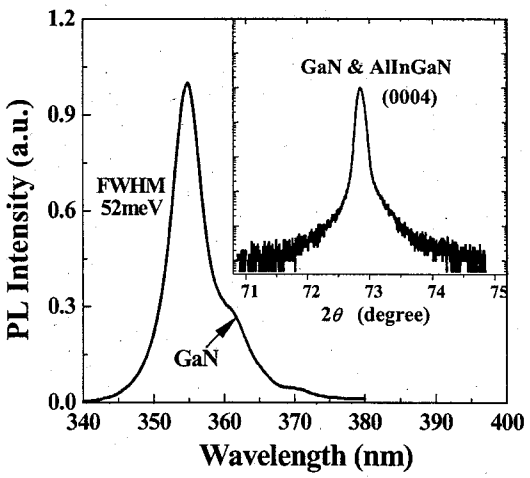

Fig.4.2.1-1 PL spectrum of S1 at room temperature. The insect shows XRD (0004) ω~2θ scan of above structure.

we believe that the thick AlInGaN layer is practically unstrained. Hall measurement indicated that the sample exhibited n type property; sheet carrier densities were 3.2×10^{12} cm^{-2} and 2.2×10^{12} cm^{-2}, electron mobilities were $432cm^2/Vs$ and $826cm^2/Vs$ at room temperature and 77K, respectively.

High-work-function Pd and Ni were selected as Schottky contact metal, respectively. Before fabricating SBDs, the samples were ultrasonically degreased in acetone and methanol, the surface oxides were removed in boiling aqua regia for 30 min and rinsed in deionized water. Then, Ti/Al/Ni/Au layers were formed by electron beam evaporation using conventional lift-off technique on the sample, which followed by annealing at 750°C for 30 s in nitrogen ambient to obtain ohmic contact. Finally, Pd/Ti/Au and Ni/Au Schottky contact dots with 150 μm diameter were patterned respectively using photoresist lift-off technique. Prior to transferring the sample into the evaporation chamber, the samples were dipped in $HCl:H_2O$ (1:1) etchant for 1 min to remove possible oxide on the surface.

The current-voltage (I-V) properties of the SBDs were measured at room temperature using Agilent 4156C semiconductor analyzer. The series resistances were found to be about ~280 Ω for two types of diodes. The typical semilog forward characteristics are shown in Fig. 4.2.1-2, its behavior can be described using thermionic emission model[21]:

$$J = J_S\left[\exp(qV/nkT)-1\right] \qquad (4.1)$$

where J_S is the saturation current density, n is ideality factor and the other symbols have their usual meanings. Schottky barrier height (SBH) and n can be obtained from experimentally available values: J_S (intercept on vertical axis of semi-log J vs V plot) and the slope value of V vs ln$J$.

$$\phi_{I-V} = (kT/q)\ln\left(A^{**}T^2/J_S\right) \qquad (4.2)$$

$$n = (q/kT)\frac{\partial V}{\partial(\ln J)} \qquad (4.3)$$

where A^{**} is effective Richardson constant and ϕ_{I-V} is barrier height. A theoretical value of the Richardson constant can be calculated using $A^{**} = 4\pi m^* qk^2/h^3$, where h is Planck's constant

and m^* is the effective electron mass for $Al_xIn_{0.02}Ga_{0.98-x}N$, which can be estimated by a linear extrapolation from the theoretical values of AlN, InN and GaN[22,23]. The uncertainty in A^{**} will result in very little error in the value of $\phi_{I\text{-}V}$, since an error of a factor of 3 in A^{**} gives rise to an error of only about kT.

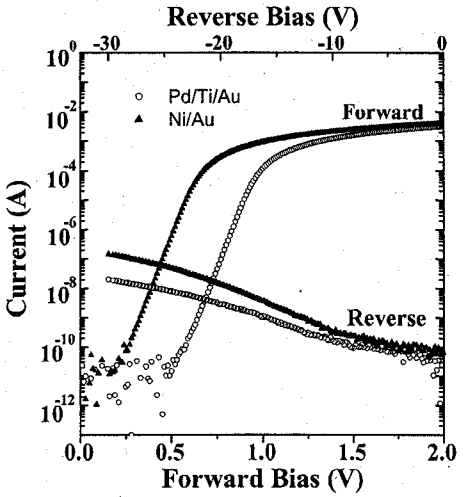

Fig.4.2.1-2. Forward and reverse I-V characteristics of both Pd/Ti/Au and Ni/Au contact Schottky diodes on S1.

Using Equation 4.2-1,-2,-3, the barrier heights (ϕ_B) and ideality factor (n value) were determined to be 1.32 eV, 1.05 for Pd/Ti/Au SBDs and 0.98 eV, 1.07 for Ni/Au SBDs, respectively. The data are the average values of 10 diodes and the standard deviations for above four values are 2.1%, 0.5%, 1.7% and 2.6%, respectively. The barrier heights of AlInGaN SBDs (Ni: 0.98 eV, Pd: 1.32 eV) did not correlate with the metal work functions (Ni: 5.15 eV, Pd: 5.12 eV). Similar phenomenon was found by Guo et al[24], which was considered to be due to the interfacial interactions between the Ni and semiconductor.

The reverse characteristics were also shown in Fig. 4.2.1-2, the leakage current for Pd/Ti/Au SBDs is lower as 2×10^{-8}A (1.1×10^{-4} A/cm^2) at a high reverse bias of 30V and is about 1 order lower than that of Ni/Au SBDs, which maybe due to the lower barrier height of Ni/Au SBDs. Strong breakdown was not observed up to the reverse bias of 90V for both devices. The I-V characteristics indicated that near ideal and high performance SBDs had been achieved.

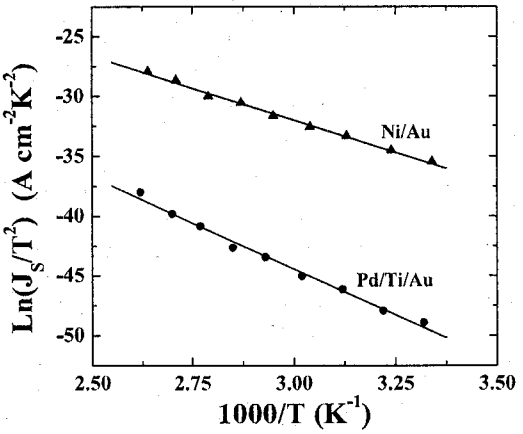

Fig.4.2.1-3. Richardson plot [ln(J_S/T^2) vs 1000/T] of Pd/Ti/Au and Ni/Au Schottky diodes on S1.

To confirm the barrier height of these SBDs, we also measured the temperature dependence of forward I-V characteristics

(I-V-T). Fig.4.2.1-3 shows Richardson plot [$\ln(J_s/T^2)$ vs 1000/T] of Pd/Ti/Au and Ni/Au SBDs, from which the barrier height and Richardson constant can be calculated using the Equ.4.2. The barrier heights are consistent with that of room temperature I-V measurement. However, the Richardson constant were smaller than that of theoretical value, which may be due to the decrease of effective contact area[25].

Capacitance-voltage (C-V) measurements were performed using HP4845A LCR at a frequency of 1MHz. Both metals SBDs exhibited similar C-V characteristics. However, we could not obtain the barrier height value from it because of the nonlinear relation of $1/C^2$ vs V. Fig. 4.2.1-4 shows a typical C-V plot of Pd/Ti/Au SBD, the capacitance decreased fast with increasing the reverse bias up to 5V; almost kept constant during the range of 5-20V; and decreased again when the bias was above 20V. This behavior is different with that of SBD on bulk GaN, which was also shown in Fig. 4.2.1-4 (closed circle) for comparison. We attribute the difference to the formation of 2DEG at the AlInGaN/GaN interface. The fast decrease of capacitance at low bias is due to the increasing thickness of depletion space charge region in the thick AlInGaN layer. With increasing the bias, the depletion region reached the AlInGaN/GaN interface and the electron of 2DEG began to be depleted. The depletion region would no. change until the whole 2DEG was pulled away, thus, the capacitance would keep constant during this period. With further increasing the bias, the depletion region passed the hetero-interface and penetrated into underlying GaN layer, which resulted in the continuous decrease in capacitance. The formation of 2DEG is further confirmed by the depth dependence of electron concentration profile[26] calculated from above C-V plot (see the inset of Fig. 4.2.1-4). The peak of electron concentration of 9.5×10^{18} cm^{-3} at

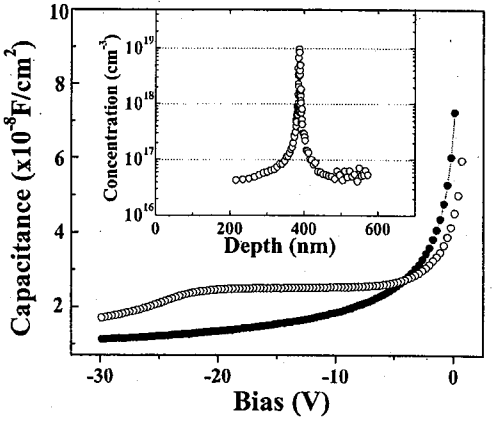

Fig.4.2.1-4. C-V characteristic of Pd/Ti/Au Schottky diode on SI (open circle) and Schottky diode on bulk GaN (closed circle). Inset shows electron concentration profile in AlInGaN/GaN structure calculated from the C-V curve.

about 390nm below the surface corresponds to the location of 2DEG channel formed at AlInGaN/GaN interface. The sheet carrier density obtained from the integration of above carrier profile[26] was about 3.7×10^{12} cm^{-2}, which was consistent with the data of Hall measurement.

In comparison with polarization effect, the conduction band offset in our sample would contribute less to the formation of 2DEG, because both AlInGaN and GaN layer were undoped and the value of conduction band offset is very small (The band gap difference between AlInGaN and GaN obtained from the PL measurement was small as 63meV). Thus, we believe that the formation of 2DEG was assigned to the existence of large spontaneous polarization in strain-free AlInGaN layer.

4.2.2 Aluminium composition dependent properties of Schottky contact on AlInGaN

4.2.2-A. Material characterization

PL spectra of the four samples (S1~S4) were shown in Fig. 4.2.2-1a, in which a strong band edge emission was observed at room temperature with a shoulder peak at longer wavelength corresponding to the emission from underlying GaN layer. As expected, the band gap energy increased with increasing Al mole fraction. However, clear differences can be observed between the theoretical prediction (Vegard's Law) and the experimental data (see Fig. 4.2.2-1b). Furthermore, the FWHM values of emission peaks increased from 53 to 83 meV with increasing Al mole fraction, implying the increase in alloy compositional disorder.

The structural properties of the four samples were characterized using XRD. The lattice mismatch between AlInGaN and GaN increased with the incorporation of Al as shown in the (0004) ω-2θ scans (see Fig. 4.2.2-2a). Figure 4.2.2-2b shows XRD asymmetrical reciprocal space mappings obtained from four AlInGaN/GaN heterostructures around $(20\bar{2}4)$. It could be seen that the epilayers had almost the same in-plane lattice constants as the GaN template, implying that coherent growth was occurring and that the strain relaxation of the AlInGaN layers was negligible. It is worth noting that the diffraction of the quaternary peak (see Fig. 4.2.2-2a) and spot (see Fig. 4.2.2-2b) overlapped with that of GaN in S1, indicating the lattice matching in the heterojunction. Thus, it can be concluded that the tensile strain in quaternary

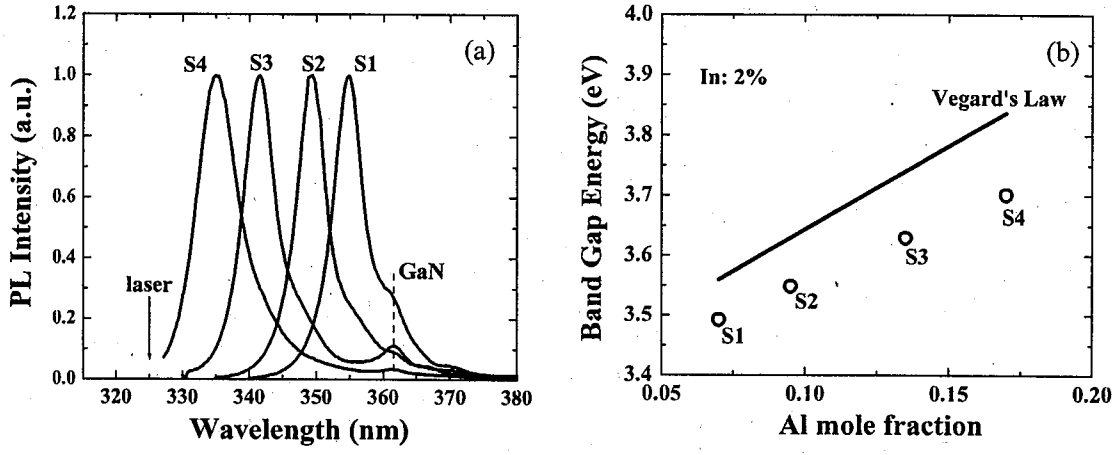

Fig.4.2.2-1 (a) PL spectra of 4 AlxIn0.02Ga0.98-xN/GaN heterostructures at room temperature. (b) Plot of bandgap of AlxIn0.02Ga0.98-xN versus Al mole fraction, in which the solid line shows extrapolated results assuming the validity of Vegard's Law.

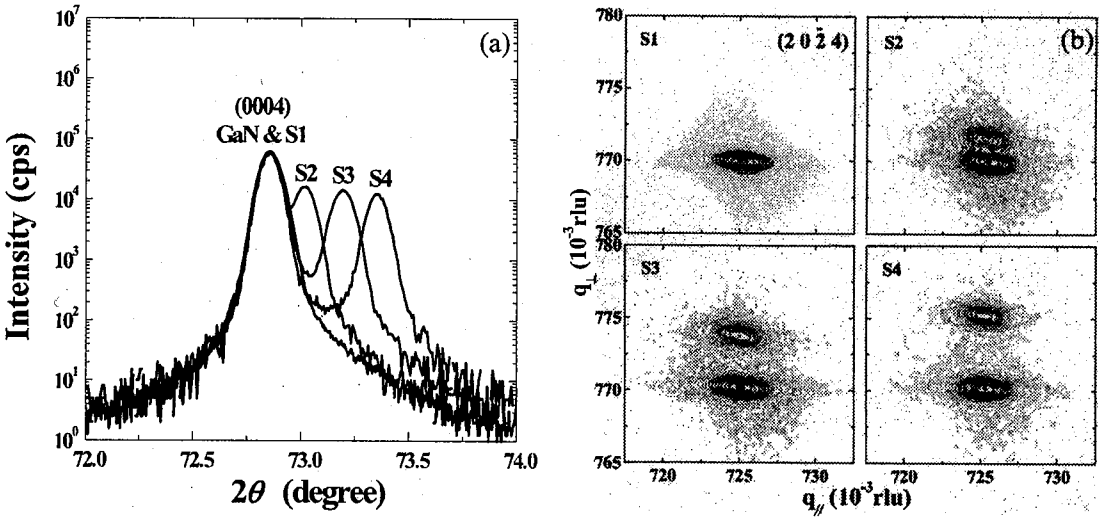

Fig4.2.2-2 XRD results of four AlxIn$_{0.02}$Ga$_{0.98}$-xN/GaN heterostructures for (a) ω-2θ scans for (0004) plane (b) asymmetrical reciprocal space mappings around.

epilayers increased from S1 to S4, which could result in the enhancement of the piezoelectric polarization in the quaternary epilayers. The high crystalline qualities of the 4 quaternary samples were confirmed from the FWHM values of the ω scans for (0004) and (20$\bar{2}$4) planes together with those of the PL spectra. This conclusion was consistent with the results of AFM measurements (not shown), which revealed that growth was occurring in the

step-flow mode with root mean square (RMS) roughness less than 0.5 nm. RMS value was found to be independent from the Al mole fraction.

To investigate the electronic properties of AlInGaN/GaN heterostructures, Hall measurements were performed using standard Van der Pauw geometry. The films were all n type and the room temperature sheet carrier concentration (n_{sh}) increased from 3.2×10^{12} to $4.1\times10^{13}cm^{-2}$ (see Table II), which is possibly due to the increased 2DEG density at the heterointerface created by the increased conduction band offset and polarization (both spontaneous and piezoelectric) in the AlInGaN layer. However, the mobility (μ_H) values did not increase monotonously with sheet carrier density. Further understanding of the phenomenon is expected after the C-V measurements.

Table II. The material properties and SBDs propterties of $Al_xIn_{0.02}Ga_{0.98-x}N$.

	Al mole fraction	PL (meV)	XRD (arcsec)		Hall		*Ideality factor*	$q\phi_{I\text{-}V}$ *(eV)*	$q\phi_{C\text{-}V}$ *(eV)*	$L_{depletion}$ *(nm)*	N_d $(10^{18}cm^{-3})$
			(0004)	$(20\bar{2}4)$	n_{sh} $(10^{13}cm^{-2})$	μ_H $(cm^2V^{-1}s^{-1})$					
S1	0.070	53	N.A.	N.A.	0.32	432	1.05	1.32	1.62	224	0.05
S2	0.095	54	237	616	0.47	655	1.14	1.26	1.58	130	0.095
S3	0.135	61	258	632	0.85	577	1.28	1.21	1.81	103	0.17
S4	0.170	83	208	510	4.1	312	1.73	1.12	2.06	23	2.06

4.2.2-B. Schottky diodes properties

(1) I-V characteristics

As shown in Fig.4.2.2-3a, the J_S and the slope of V vs ln$J$ increased from S1 to S4, indicating a decrease in $\phi_{I\text{-}V}$ and an increase in n. Figure 4.2.2-4 shows the plots of $\phi_{I\text{-}V}$ and n as a function of Al mole fraction. The result is an average of the data from 10 SBDs for each sample. According to Schottky-Mott theory[27], the barrier height of an SBD should follow

$$q\phi = \phi_m - \chi_s \qquad (4.4)$$

where ϕ_m is work function of metal and χ_s is electron affinity of semiconductor. The electron affinity of $Al_xIn_{0.02}Ga_{0.98-x}N$ (χ_q) can be calculated assuming a linear dependence (Vegard's Law) of electron affinity (χ_{AlN}=2.05eV [28], χ_{GaN}=4.2eV) on x as

$$\chi_q = (0.02\cdot\chi_{InN} + 4.116) - 2.15\cdot x \qquad (4.5)$$

where χ_{InN} is still unavailable from the open literature. It can be seen that χ_q decreases with increasing x, which indicates that the Schottky barrier height of $Al_xIn_{0.02}Ga_{0.98-x}N$ increases with x (see Eq. 4.5). This seems to contradict the results obtained from the I-V measurements (see Fig.4.2.2-4). The dependence of the ternary AlGaN Schottky barrier height on Al mole fraction has been investigated by many groups[29-35], and all the results were in agreement with Schottky-Mott theory. We believe the conflict in our case is due to the deviation of AlInGaN SBDs properties from an ideal Schottky diode, as demonstrated by the dependence of the ideality factors on the Al mole fraction (see Fig. 4.2.2-4). The calculation of ϕ_{I-V} is based on the thermionic emission model, in which the current flow is only due to thermionic emission and the ideality factor n is near unity. With an increase in n, the barrier height obtained from Eq. (4.2) would deviate from the true value.

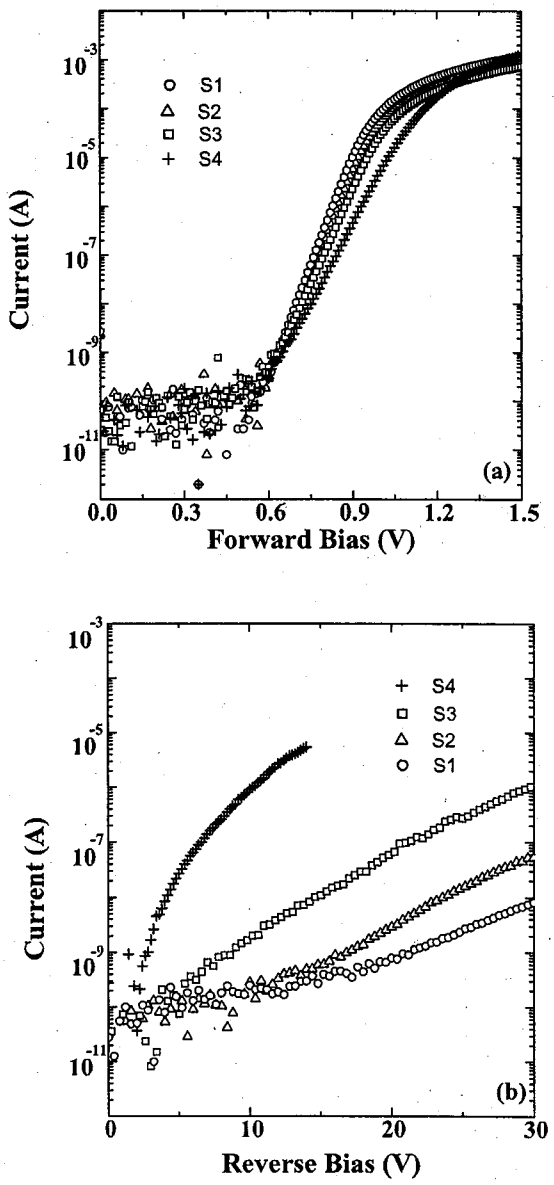

Fig4.2.2-3 (a) Forward and (b) reverse I-V characteristics of Pd/ $AlxIn_{0.02}Ga_{0.98-x}N$ Schottky diodes.

Figure 4.2.2-3b shows the typical reverse characteristics of the 4 types of SBD. The increase in leakage current was observed in high Al mole fraction samples. Strong breakdown was not observed up to the reverse bias of 90V except for S4, which broke down at 15V.

(2) C-V characteristics

To further understand the nature of $Al_xIn_{0.02}Ga_{0.98-x}N$ SBDs, C-V measurements were performed, from which the Schottky barrier height can be also obtained (see Fig. 4.2.2-5) by using the linear relationship[27] between $1/C^2$ and bias V

$$\left(1/C^2\right)=\left(2/qN_d\varepsilon_0\varepsilon\right)\cdot\left(\phi_{C-V}-\xi-V-kT/q\right) \qquad (4.6a)$$

$$\xi=\left(kT/q\right)\cdot\ln(N_c/N_d) \qquad (4.6b)$$

where C is the measured differential capacitance per unit area and ε is the dielectric constant of $Al_xIn_{0.02}Ga_{0.98-x}N$, which was estimated by a linear extrapolation from the ε value of AlN, InN and GaN assuming the validity of Vegard's law. ξ is the potential measured from Femi level to conduction band edge; N_c is the conduction-band effective state density of $Al_xIn_{0.02}Ga_{0.98-x}N$, which is related to the effective electron mass of semiconductor; N_d is the ionized donor concentration, which is related to the slope of $1/C^2$ vs V. Figure 4.2.2-5 shows the typical plots of $1/C^2$ versus V for 4 samples. The solid lines are the linear fitting results for the data of $1/C^2$ obtained for biases in a small range. The barrier height $\phi_{C\text{-}V}$ was obtained from

$$\phi_{C-V}=V_i+\xi+kT/q, \qquad (4.7)$$

where V_i is the intercept of the linear fitting line with the horizontal axis. It is worth mentioning that the C-V data are independent of frequency between 10 kHz and 1 MHz.

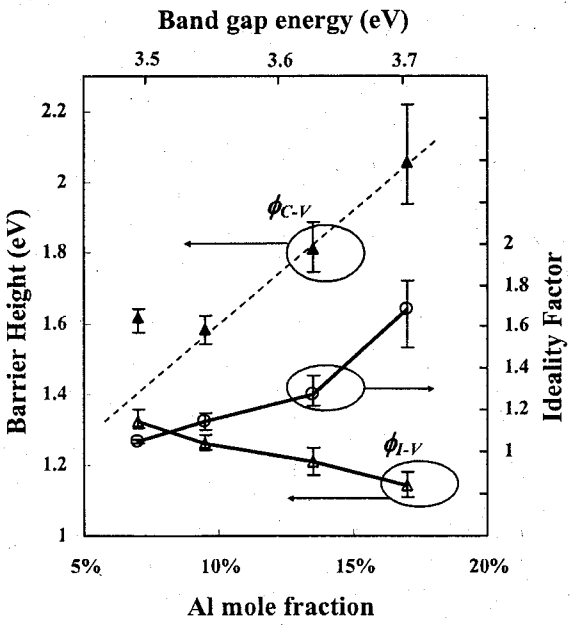

Fig4.2.2-4 Plot of barrier height and ideality factor of $Pd/Al_xIn_{0.02}Ga_{0.98-x}N$ Schottky barrier diodes versus Al mole fraction; the dash line is a guide for the eye. All the results are the average value from 10 devices.

Obviously, the dependence of measured $1/C^2$ data on the bias voltage gradually deviated from linearity with decreasing Al mole fraction (see Fig.

4.2.2-5), indicating the inhomogeneous carrier distribution. Therefore, it is necessary to calculate the carrier profiles by using the C-V profiling technique, which allows one to measure the carrier concentration[35]

$$n_e = \left(C^3/q\varepsilon_0\varepsilon\right)\cdot\frac{dV}{dC} \qquad (4.8)$$

as a function of depth

$$z = \varepsilon_0\varepsilon/C\,, \qquad (4.9)$$

where V is the voltage applied to the Schottky contact. To obtain the full carrier profile, a reverse bias of between 0 and 40V was applied to the SBDs, except for the SBDs in S4 because of the lower breakdown voltage (less than 15V). As shown in Fig. 4.2.2-6, a high density 2DEG was formed at the heterointerface and increased with Al mole fraction, which resulted from the increase in the conduction band offset and the polarization (both piezoelectric and spontaneous) in the AlInGaN. It should be noticed that the formation of 2DEG in S1 is mainly due to the spontaneous polarization (see *Section 4.2.1*) because of the small conduction band offset value and negligible strain at the heterojunction. Besides the 2DEG peak, a flat carrier concentration profile can also be observed in the shallow AlInGaN region, which corresponds to the background doping in the bulk quaternary region, since all the $Al_xIn_{0.02}Ga_{0.98-x}N$ samples were unintentionally doped. It can be seen that,

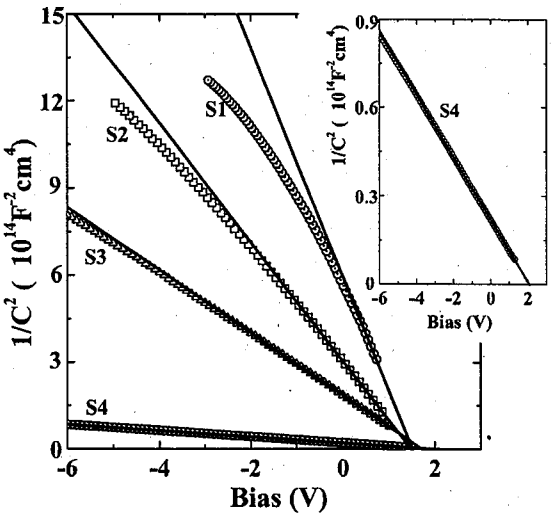

Fig4.2.2-5.Plot of $1/C^2$ versus V for Schottky diodes fabricated from $Al_xIn_{0.02}Ga_{0.98-x}N$/GaN structures. The solid lines are the linear fitting results for the $1/C^2$ data at a small bias range. The inset is a magnified $1/C^2$ plot of S4.

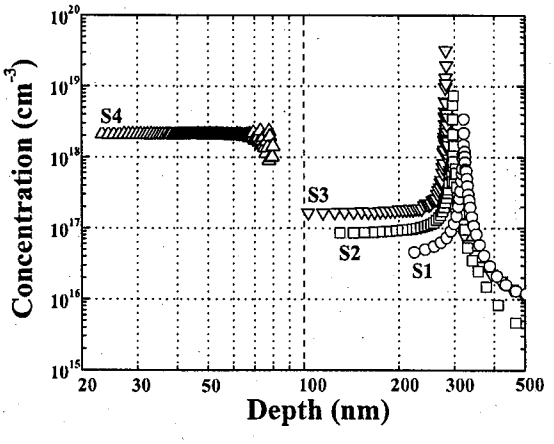

Fig4.2.2-6. Carrier concentration profiles in the $Al_xIn_{0.02}Ga_{0.98-x}N$/GaN structures calculated from C-V measurements

with the increase of Al mole fraction, the background doping in the $Al_xIn_{0.02}Ga_{0.98-x}N$ increased from 10^{16} to 10^{18} cm^{-3}. This suggests that, besides the formation of 2DEG, high density background donors in AlInGaN epilayer also leads to the increase in sheet carrier density obtained from the Hall measurements. Therefore, Hall mobility values were resulted from the parallel conduction of both quaternary layer and 2DEG. The lower mobility value in high-Al sample can be explained in terms of the scattering from the high density background donors. In addition, due to the increase of the background donor concentration, the depletion length decreased from about 200 nm in S1 to 20nm in S4 (see Fig. 4.2.2-6), resulting in a narrowing of the barrier width as the Al mole fraction increased.

It is worth noting that the 2DEG profile of S4 could not be available because of the existence of high density background donors, which resulted in the large leakage current and early breakdown (see Fig. 4.2.2-3b). The origin of background donors is still unclear. It may be attributed to the native defects or impurities related to the Al incorporation. Further effort is needed to reduce and understand the background donor, since it will deteriorate the performance of Schottky diode and HFET.

In Fig. 4.2.2-4 the Al mole fraction dependence of $\phi_{C\text{-}V}$ agrees well with the prediction of Schottky-Mott theory except for the S1. We believe that the barrier height obtained from C-V measurement is much closer to the true barrier height, since the data obtained in C-V measurements are extrapolated to $1/C^2=0$ corresponding to near flat-band conditions. $\phi_{C\text{-}V}$ is also called flat-band barrier height. With respect to the $\phi_{C\text{-}V}$ value of S1, we believe it has very larger error, because inaccurate (larger) value of bulk carrier concentration (near the heterointerface) was used to calculate the barrier height. As shown in Fig. 4.2.2-6, the carrier distribution in AlInGaN region becomes more homogeneous with distance from the heterointerface. Obtaining an accurate carrier density for the bulk quaternary in S1 is impossible by C-V measurement because of its longer depletion length (about 220 nm) in the quaternary region. Let it be supposed that much more accurate carrier density (lower density) can be detected; a larger absolute slope value of the linear fitting line (see Fig. 4.2.2-5) will be available, by which the horizontal intercept of V_i will significantly decrease. Thus, the $\phi_{C\text{-}V}$

value will decrease a lot although ξ increases slightly due to using a lower N_d value (see Eq. 4.7). N. Kubota et al[10] proposed a method to deduce the $\phi_{C\text{-}V}$ of n-GaN with inhomogeneous carrier concentration profile, by which nearly 0.2 eV decrease in $\phi_{C\text{-}V}$ was found in comparison with linear fitting method.

4.2.2-C. Discussion

As shown in Fig. 4.2.2-4, the I-V behavior of Schottky diode deviated from an ideal one with increasing Al mole fraction, which was accompanied by an increase in the difference between $\phi_{C\text{-}V}$ and $\phi_{I\text{-}V}$. In fact, many factors may result in such abnormity of I-V behavior, such as (i) interface states at a thin oxide layer between the metal and the semiconductor[37]; (ii) generation/recombination within the depletion region[27] (n=2); (iii) tunneling effects in highly doped semiconductors[27, 38]; (iv) image force lowering of the Schottky barrier[39] and (v) Inhomogeneous Schottky barrier[40, 41]. We believe that the item (i) and (ii) are inappropriate to explain our experiment data, because the C-V data is independent from the frequency[41] and the surface oxides of all samples was believed to be removed after dipping the samples in aqua regia for 30 min.

Due to the existence of large density background donors in high-Al contained sample, it seems to explain the abnormity easily in terms of tunneling effect and image force effect, since both effects depend on carrier density. However, it is not true if we estimate the magnitude of these effects.

(1) Tunneling Effect

According to Field and thermionic-field emission theory[27], the barrier lowing $\Delta\Phi_{tunn}$ caused by tunneling effect is given by

$$\Delta\Phi_{tunn} = (1.5E_{00})^{2/3} V_d^{1/3} \qquad (4.10)$$

where V_d is built in potential of Schottky diode and $E_{00} = \frac{\hbar}{2}\sqrt{N_d / m^* \varepsilon\varepsilon_0}$ is characteristic parameter of tunneling. The largest $\Delta\Phi_{tunn}$ in S4 can be estimated to be less than 10 meV by knowing effective mass (~0.22m_0), dielectric constant (~10), carrier concentration (~10^{18}cm^{-3}) and built in potential (~1 V), which implies the tunneling effect plays a negligible role in the

transport.

(2) Image force lowing of Schottky barrier

The barrier lowing $\Delta\Phi_{img}$ caused by image force effect can be estimated by[27]

$$\Delta\Phi_{img} = \sqrt{qE_{\max}/4\pi\varepsilon\varepsilon_0} \qquad (4.11a)$$

$$E_{\max} = (2qN_d/\varepsilon\varepsilon_0)^{1/2}\sqrt{V_d - kT/q}\,, \qquad (4.11b)$$

where E_{max} is the maximum electric field in the depletion region. The largest barrier lowing in S4 due to the high background doping up to 2×10^{18} cm^{-3} is estimated to be 0.1 eV, which can not explain nearly 1 eV difference between the $\phi_{C\text{-}V}$ and $\phi_{I\text{-}V}$ in S4.

(3) Inhomogeneous Schottky barrier

Another possible reason that results in large difference between I-V and C-V measurements is barrier inhomogeneirtes[40, 41]. In this theory it is believed that any spatial variation in the barriers will cause the current flow preferentially through the barrier minma, while barrier height measured by C-V method is the mean value of the variation. Therefore one will expect intuitively that $\phi_{I\text{-}V}$ is smaller than $\phi_{C\text{-}V}$. The barrier difference between the two measurements was expressed as[40]:

$$\Delta\Phi_{ihg} = \sigma_E{}^2/(2kT/q) \qquad (4.12)$$

where σ_E is standard deviation of average built in potential V_d of Schottky diode. The barrier inhomogeneities may originate from the interface roughness of Schottky contact or alloy compositional disorder[31] in multi-element compound semiconductors. We believe that the barrier inhomogeneities of AlInGaN may mainly attributed to the alloy compositional disorder since the surfaces of AlInGaN were observed to be atomically flat and the roughness were independent of Al mole fraction. Normally the level of alloy compositional disorder is characterized by a standard deviation of band tail potential fluctuation σ, which may be deduced from the plot of temperature dependent bandgap[42, 43]. The magnitude of σ_E and σ should be close to each other although their definitions are not exactly same. Bell et al[43] found

that the σ value in $Al_yGa_{1-y}N$ increased from 7 meV at y=5% to 21 meV at y=25%, indicating the increase of alloy disorder with Al incorporation. In this work, the increased PL FWHM value from 53 to 83 meV with Al incorporation is one of the evidence of the enhancement of compositional disorder. The σ value of S2 was estimated to be about 9 meV in our previous work (see the Table I in section 2.1). Therefore by referencing the change of σ in ref. 43, we can estimate the σ value of S4 will not increase too much even the Al mole fraction was increased up to 17%. If the nearly 0.9 eV (excluding ~0.1 eV of image force effect) difference between $\phi_{C\text{-}V}$ and $\phi_{I\text{-}V}$ in S4 is attributed to the barrier inhomogeneities, the σ value (see Eq. 4.12) should be more than 210 meV, such high σ value is obviously too unreasonable to account for the barrier inhomogeneities caused by alloy compositional disorder in AlInGaN. In ref. 31 the difference between the $\phi_{C\text{-}V}$ and $\phi_{I\text{-}V}$ of $Al_{0.2}Ga_{0.8}N$ Schottky diodes, which was verified to be due to the barrier inhomogeneities caused by Al compositional disorder, was only about 0.2 eV,

(4) Polarization effect

According to the above discussion, it is clear that the traditional electron transport mechanisms of Schottky diode can not quantitatively explain the abnormity, which indicate that the electron transport in AlInGaN/GaN Schottky diode is dominated by another mechanism. Here we propose that the increased difference between $\phi_{C\text{-}V}$ and $\phi_{I\text{-}V}$ with Al incorporation may be due to polarization effect in AlInGaN. The Schottky diodes in this study are fabricated on fully strained AlInGaN/GaN heterojunction structure, not on a bulk semiconductor. Tensile strain in AlInGaN layer increased with the increase of Al mole fraction (see Fig. 4.2.2-2), which resulted in the enhancement of polarization effect.

Actually, many studies revealed that barrier height (obtained by I-V measurement) of Schottky Diode on strained $Al_yGa_{1-y}N$ /GaN HFET structure is as low as 0.5~0.87 eV[44-49] at y=22~40 % with very large ideality factor[47-49] ranged in 1.7~4.0, such SBH values are considerably lower than those of $Al_xGa_{1-x}N$ bulk structure[29-35] (obtained by either C-V or I-V method), which is several microns thick and is fully relaxed. E. Monroy[29] et al summarized

these published $\phi_{C\text{-}V}$ value of bulk $Al_yGa_{1-y}N$ Schottky diodes, and showed that the SBH increased from 1 to 2 eV with the increase of y value from 0 to 35%. Z. Lin et al[50] pointed out that, due to the existence of strong polarization effect, the SBH of strained AlGaN/GaN HFET can not be determined by conventional thermionic emission theory (I-V measurement), which would yield a large error.

In $Al_yGa_{1-y}N$/GaN HFET structure, $Al_yGa_{1-y}N$ barrier layer is commonly 20 ~ 30 nm thick and is proven to be free from relaxation even if *y* value is as high as 40%[51]. Due to the thin barrier layer and the formation of high density 2DEG caused by strong polarization effect, the flat carrier concentration profile in the thin $Al_yGa_{1-y}N$ layer can not be observed in the C-V measurement. Thus, a C^{-2} versus V plot would not yield a straight line. Therefore the C-V measurement also can not be utilized to deduce the SBH of $Al_yGa_{1-y}N$/GaN HFET structure. Based on this point, photoemission technique was proposed in ref. 52, by which the SBH of $Al_yGa_{1-y}N$/GaN HFET structure was deduced to be 1.29, 1.52 and 1.56 eV for y=15%, 25% and 30%[52, 53], respectively. Such values are also fairly larger than that published I-V results[44-49] although the authors did not give $\phi_{I\text{-}V}$ for comparison in their studies. Commonly, both photoemission and C-V method are thought to be accurate way to deduce the SBH[54] in comparison with I-V method.

Based on above discussion, we propose that, due to the enhancement of polarization effect with Al incorporation, the I-V behavior of Schottky diode on the strained $Al_xIn_{0.02}Ga_{0.98-x}N$/GaN strongly deviates from the thermionic emission theory. The deviation yielded a large error in barrier height value, which gave an opposite Al dependent tendency in comparison with the prediction of Schottky-Mott theory. On the other hand, the acquirement of $\phi_{C\text{-}V}$ value from Schottky diodes on the strained $Al_xIn_{0.02}Ga_{0.98-x}N$/GaN is attributed to the thick layer of $Al_xIn_{0.02}Ga_{0.98-x}N$, which is 10 times thicker than that of $Al_yGa_{1-y}N$ barrier layer in $Al_yGa_{1-y}N$/GaN HFET structure and is also thicker than depletion length of Schottky barrier. Thus, the carrier profile in AlInGaN layer could be observed by C-V measurement, in which a C^{-2} versus V plot yielded a straight line (see Fig. 4.2.2-5). Due to the accuracy of C-V method in obtaining SBH, the tendency of Al dependent $\phi_{C\text{-}V}$ was consistent with the

prediction of Schottky-Mott theory, which resulted in a large difference between $\phi_{C\text{-}V}$ and $\phi_{I\text{-}V}$. To date the electron transport mechanism in Schottky interface related to polarization effect is still unclear, which is expected to be explored.

4.2.2-D. Brief Summary

Pd Schottky barrier diodes were fabricated on undoped $Al_xIn_{0.02}Ga_{0.98-x}N$/GaN heterostructures with different x values less than 20%. The material properties characterized by PL, XRD and AFM indicated that the quaternary samples were coherently grown on GaN template with high crystalline quality. The flat band barrier height obtained by C-V measurement increased in high-Al samples up to 2.06 eV, which agreed well with the prediction of Schottky-Mott theory. Furthermore, both an increase in background donor concentration and enhanced high-density 2DEG profiles were also observed in C-V measurements as the Al mole fraction was increased. However, the I-V behaviors deviated from that of an ideal Schottky diode with Al incorporation, which was accompanied by an increase in the difference between $\phi_{C\text{-}V}$ and $\phi_{I\text{-}V}$ up to nearly 1 eV. The large difference of barrier height between I-V and C-V measurement could not be quantitatively explained by traditional electron transport mechanisms of Schottky diode, such as tunneling effect, image force effect and barrier inhomogeneities theory. Strong polarization effect in strained $Al_xIn_{0.02}Ga_{0.98-x}N$/GaN heterostructure is proposed to account for the results, since similar phenomena had been observed extensively in strained $Al_yGa_{1-y}N$/GaN heterojunction structures.

4.3 Quaternary AlInGaN based Heterostructure Field Effect Transistors

Epilayers of quaternary AlInGaN were grown by MOCVD on c-plane sapphire substrates. After the growth of 3 μm i-GaN, about 30 nm undoped AlInGaN was deposited at 900 °C. Before the device processing, the heterostructures were characterized by XRD technique, photoreflectance (PR) measurements and Hall measurements.

The device isolation was accomplished by mesa dry etching down to i-GaN by BCl_3 plasma reactive ion etching. Then, 100-nm-thick SiO_2 passivation layer was deposited by

electron beam evaporation. The Ti/Al/Ni/Au (15/70/12/40 nm) and Pd/Ti/Au (40/20/60 nm) were deposited as Ohmic contact and Schottky gate contact, respectively. The dimensions of the devices used in this report are as follows: source-drain distance (L_{sd}) = 8 μm; gate width (W_g) = 15 μm; gate length (L_g)= 2 μm and source-gate distance (L_{sg})= 3 μm. The dc characteristics were measured using Agilent 4156c semiconductor parameter analyzer. To measure the 2DEG density as a function of channel depth, C-V measurements were carried out at 1 MHz on Schottky diodes using HP4845A inductance, capacitor and resistance meter.

4.3.1 Properties of $Al_xIn_{0.02}Ga_{0.98-x}N$ /GaN HFET with different x value

Four samples of $Al_xIn_{0.02}Ga_{0.98-x}N$ were grown with 2% In mole fraction and different x value (10, 17, 22, and 31%). Hereinafter, the four samples are referred to as S_A, S_B, S_C, and S_D, respectively, with increasing the Al mole fraction.

Figure 4.3.1-1 shows the XRD asymmetrical reciprocal lattice mappings of four heterostructures, in which the same in-plane lattice constant between AlInGaN and GaN revealed that the coherent growths of AlInGaN barrier layers were obtained. Moreover, the decreased out-of-plane lattice constant from S_A to S_D indicated that the tensile in-plane strain in AlInGaN epilayer increased with the Al incorporation, which would result in an increase of piezoelectric polarization field in AlInGaN layer. It is worth mentioning that the in-plane strain in S_D is similar to that in $Al_{0.26}Ga_{0.74}N$ /GaN HFET structure [54]. The bandgap (E_g) of AlInGaN estimated by PR measurement [55] was found to increase from 3.628, 3.804, 3.887 to 4.058 eV, respectively, with increasing the Al mole fraction. Room temperature Hall measurement revealed that the materials exhibited n type properties. An increase in sheet carrier density with Al mole fraction was observed (see Fig. 4.3.1-2), which

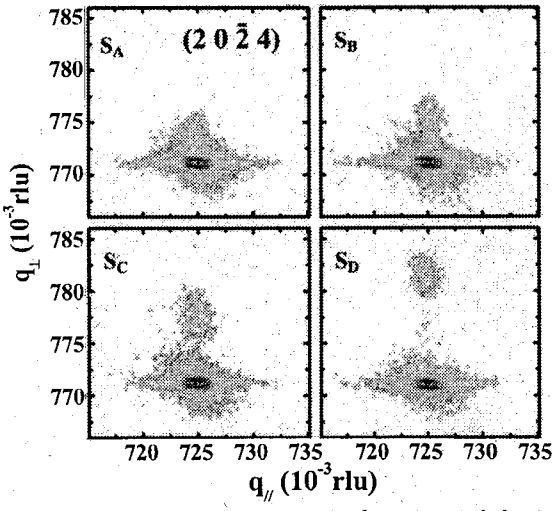

Fig4.3.1-1 XRD asymmetrical reciprocal lattice mappings around for four AlInGaN/GaN heterostructures

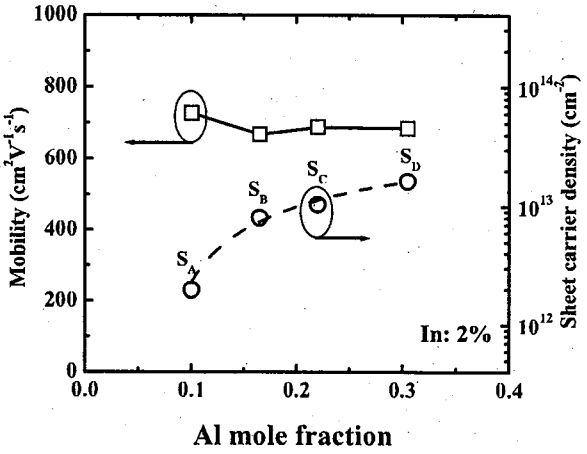

Fig4.3.1-2 The plot of mobility and sheet carrier density as a function of Al mole fraction.

may be due to the enhancement of 2DEG at the heterointerface created by the increased conduction band offset and polarization (both spontaneous and piezoelectric) in the AlInGaN layer. The enhancement in 2DEG density should be further confirmed by C-V measurement. The mobility values did not vary too much with Al content and kept at around 700 $cm^2V^{-1}s^{-1}$. The values are lower than those of conventional AlGaN/GaN heterostructures (~1000 $cm^2V^{-1}s^{-1}$) [54], which indicate that the material quality needs to be further improved.

The dc characteristics of HFETs revealed that all the HFETs exhibited good pinch off characteristics. Figure 4.3.1-3 shows the plot of drain-source current (I_{DS}) versus drain-source voltage (V_{DS}) characteristics at different values of gate-source voltage (V_g) for S_A and S_D. With increasing Al mole fraction (see Fig. 4.3.1-4), both the maximum drain current (I_{dmax}) and the peak extrinsic transconductance (g_{mmax}) increased, which was maybe due to the enhancement in 2DEG density. The largest I_{dmax} and g_{mmax} was obtained in S_D to be about 1230 mA/mm and 138 mS/mm, respectively. The I_{dmax} value was much higher than that of conventional modulation-doped $Al_{0.26}Ga_{0.74}N$ HFETs [54] that has similar device dimensions and similar lattice strain with S_D. We believed that it was attributed to the larger spontaneous polarization in AlInGaN

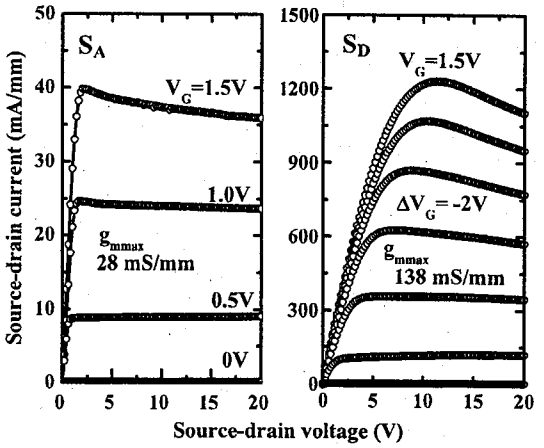

Fig4.3.1-3 The plots of source-drain current versus source-drain voltage for sample S_A and S_D

barrier in S_D, which resulted in higher 2DEG density. However, the g_{mmax} was lower (commonly ~200 mS/mm in modulation-doped AlGaN based HFET), which was maybe due to the lower Hall mobility value (689 $cm^2V^{-1}s^{-1}$) in S_D.

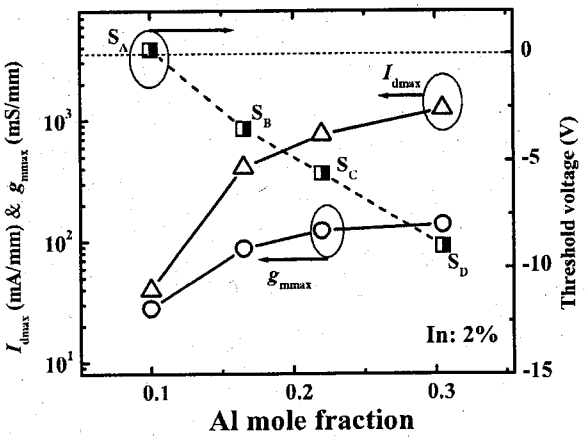

Fig4.3.1-4 The plot of HFET properties as a founction of Al mole fraction.

C-V measurements conducted on Schottky diodes of the four samples indicated that 2DEG had formed at AlInGaN/GaN interface (see Fig. 4.3.1-5), in which the peak electron concentration increased from 0.4×10^{19} to $6.5\times10^{19}cm^{-3}$ with the increase of Al mole fraction. The result was consistent with the data of Hall measurements. In addition, a flat profile with high carrier densities of ~1.5 and ~2.5×10^{18} cm^{-3} (see the circled parts in Fig. 4.3.1-5) were found in AlInGaN barrier region of S_C and S_D, respectively. We believed that such high carrier density was resulted from background doping since the AlInGaN barrier layers were all undoped. It was just the high density carrier in AlInGaN region that resulted in short depletion length, which made the carrier profile in AlInGaN region could be detected. However, the flat carrier profile in AlInGaN barrier region of S_A and S_B could not be observed due to the longer depletion length, indicating the lower carrier density in the barrier layer. In comparison with S_A, a small part of gradient carrier profile could be observed in barrier region of S_B, which could

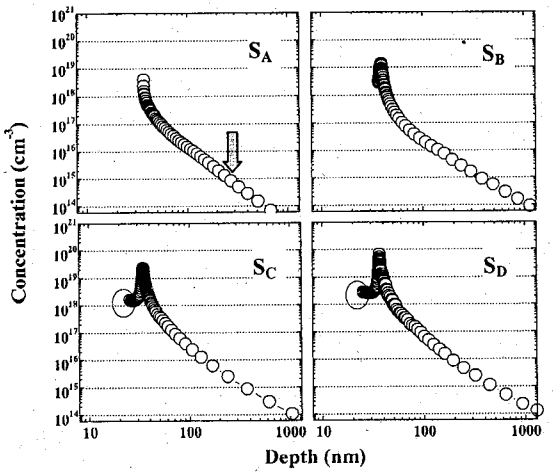

Fig4.3.1-5 The depth profile of carrier density in four heterostructures. The grey arrow in profile of S_A indicates the depletion length at zero bias, which corresponding to a very low carrier density. The circled parts in S_C and S_D are corresponding to the background doping density in the quaternary barrier layers.

not be detected in S_A. This indicated that the carrier density in the barrier region of S_B is higher than that in S_A. Therefore, the results shown in Fig. 4.3.1-5 implied that the background doping density increased with the Al incorporation from S_A to S_D. Moreover, the increased background donor density with Al incorporation was confirmed from other thicker AlInGaN/GaN samples (see section 4.2.2). Thus, we may understand that the increase in sheet carrier density obtained from the Hall measurements was not only due to the increase of conduction band offset and polarization field in AlInGaN, but also due to the increased background donor density.

The gate leakage properties for the four samples were shown in Fig. 4.3.1-6. The breakdown was not observed within the available bias range (0~100 V). Moreover, it was also found that the leakage current (I_{gs}) increased with Al incorporation, which may be attributed to the increased background doping.

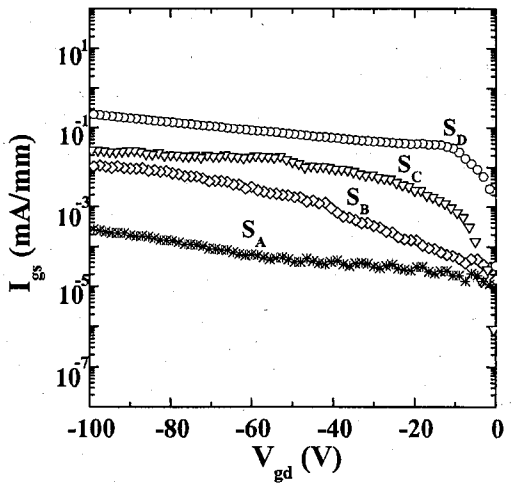

Fig4.3.1-6 The plot of two-terminal gate leakage current as a function of gate-source reverse bias for the four AlInGaN/GaN HFETs.

It is noteworthy that (see Fig. 4.3.1-4) the threshold voltage (V_{th}) strongly depended on Al mole fraction, in which normally-off HFET was demonstrated in S_A (also see Fig. 4.3.1-3). The realization of normally-off operation is due to the effective control of sheet carrier density by adjusting the polarization field. The conduction channel is easy to be pinched off when 2DEG density becomes less. As shown in Fig. 4.3.1-5, the depletion length at zero bias of Schottky diode in S_A was confirmed to be about 280 nm (marked by a gray arrow mark) by C-V measurement, which corresponds to a very lower carrier concentration of about 6×10^{14} cm^{-3}, indicating the full depletion of the channel. However, the I_{dmax} was fairly lower in comparison with that of common normally-on GaN based HFETs due to the larger channel resistance caused by both lower 2DEG density

and mobility. The performance improvement in AlInGaN HFETs (both normally-off and normally-on) may be expected by improving the material quality and optimizing the device structure, such as reducing the background donor to increase the mobility of AlInGaN/GaN heterostructure; optimizing the barrier strain by adjusting the In and Al mole fraction; optimizing the barrier thickness and reducing the gate length to increase the transconductance and so on.

The results indicate that quaternary AlInGaN is a promising candidate for high power and high frequency device applications.

4.3.2 Realization of Normally-off operation on AlInGaN based HFETs

From the application point of view, enhancement-mode HFET (E-HFET, or normally-off) is very essential since utilizing both depletion mode HFET (D-HFET) and E-HFET will significantly simplify the circuit configuration and reduce the power consumption in digital logic applications. Moreover, the normally-off operation is strongly required in high power switching application from the fail-safe point of view. To date, there is no report concerning about the realization of enhancement-mode (E-mode) operation in quaternary AlInGaN/GaN HFETs, except for few papers[56-59] about E-HFETs on AlGaN/GaN.

In comparison with D-HFETs, GaN based E-HFETs are difficult to be available due to the existence of high density two-dimensional electron gas (2DEG) at the heterointerface, which results in a non-pinched-off conduction channel at zero gate bias. For Schottky gate FETs, the only way to realize normally-off operation is to reduce the carrier density under the gate. By this way, many techniques were utilized, such as gate recessing[56], barrier layer thinning (non-gate recessing) [57], gate annealing [57], gate fluoride-based plasma treatment [58] and selectively grown pn junction gate [59]. In this section, the following two methods were utilized to realize the normally-off operation on AlInGaN HFETs.

(1) By thinning the barrier layer

The device structure was grown by MOCVD on a c-plane sapphire substrate. The epilayer consists of low temperature grown GaN buffer layer, 3-μm-thick i-GaN and an undoped

quaternary $Al_{0.3}In_{0.02}Ga_{0.68}N$ barrier. To realize the E-mode operation, the thickness of AlInGaN was adjusted and reduced in comparison with that of D-HFET, since the density of 2DEG will decrease when the barrier thickness is reduced. Three samples were grown at same condition except for the barrier thickness, which were determined to be about 7, 10 and 22 nm. The devices were fabricated in the same process with previous section without any passivation.

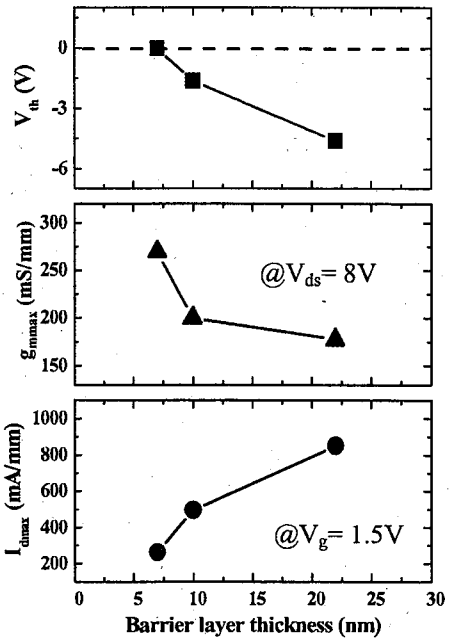

Fig.4.3.2-1. The plot of I_{dmax}, g_{mmax} and V_{th} as a function of barrier layer thickness. (L_g=2μm, W_g=15μm, L_{sd}= 8μm)

The dc characteristics of AlInGaN/GaN HFET were measured and the result was summarized in Fig. 4.3.2-1, from which one can find that the threshold voltage shifted towards the positive direction when the barrier thickness was reduced and the normally-off operation was realized when barrier layer is 7 nm. I_{dmax} value, which was obtained when gate is biased at 1.5 V, decreased correspondingly. This may be due to the sheet carrier density reduction with thinning the barrier layer. On the other hand, the maximum transconductance was increased a lot up to 270mS/mm with reducing the barrier thickness, which resulted from the increase in the Schottky junction capacitance. E-mode operation was also clearly exhibited in the DC transfer characteristics (see Fig. 4.3.2-2), in which more than 400 mA/mm of I_{dmax} value was obtained on a 2 micron-length device, when V_{gs} = 2 V. Such value is comparable to that of conventional D-mode AlGaN/GaN HFET. The threshold voltage (V_{th}) was determined to be 0.02 V if defining V_{th} as the gate bias intercept of the linear extrapolation of square root of drain current. It is worth mentioning that the data obtained above are all from the unpassivated devices. For the E-mode device with electron beam evaporated SiO_2 passivation, much current collapse was observed even at slow scanning swing condition. Such collapse can be removed under the illumination with a common bulb lamp, which indicated that much

surface traps was locating in the interface between the SiO_2 and AlInGaN surface. Further experiments are needed to understand it.

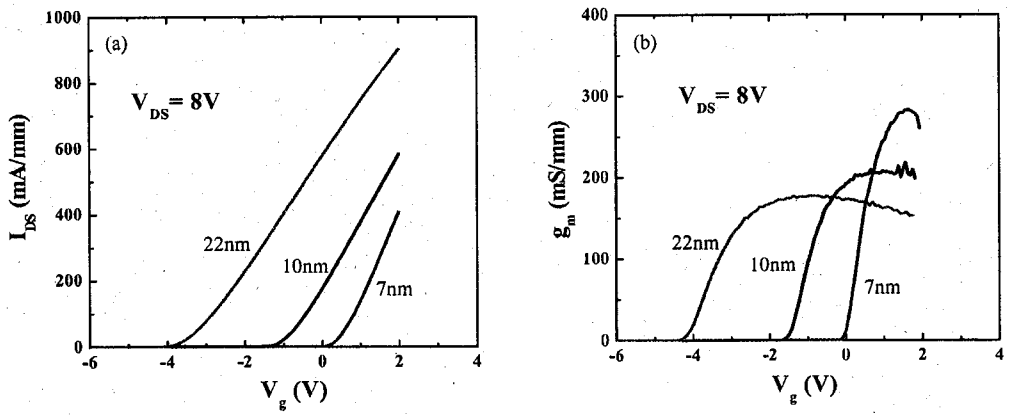

Fig.4.3.2-2.Transfer properties of three devices with different barrier thickness. (L_g=2μm, W_g=15μm, L_{sd}= 8μm)

(2) By gate recessing

Gate recessing was performed on 30 nm-$Al_{0.3}In_{0.02}Ga_{0.68}N$/GaN HFET structures. The RIE condition is same as that in isolation process. BCl_3 is used as an etchant gas, the chamber pressure is 3 Pa, plasma power is 10 W. In this experiment, 4 samples were used with different RIE etching time: 0, 40, 80, 120 sec. The etching speed was about 5-6 nm/sec, which was confirmed by AFM checking. As shown in the Fig.4.3.2-3, both I_{dmax} and g_{mmax} decreased abruptly when etching time is increasing, although the V_{th} moved towards the positive direction. This is maybe due to the etching damage in the gate region, which may be avoided by post annealing process or optimizing the RIE process.

To confirm the existence of damage, the post annealing processes were performed, in which the devices were annealed at 300 °C at N_2 ambient. Fig.4.3.2-4 shows the HFET parameters as a function of annealing time. As shown, for the 40 and 80 sec-etched devices, their properties were almost kept constant after short or long time annealing process; however, for 120 sec-etched device, both I_{dmax}, g_{mmax} increased more than several ten times after annealing processes. This indicated the existence of ion damage during the gate recessing, the longer recessing, the larger damage is. The recovery effect can also be clearly observed in Fig.4.3.2-3, in which the 6-min annealing results are shown for comparison with that of the

as-etched devices. Finally, after damage recovery process, the normally-off operation had been obtained in a 120 sec-gate recessed device with lower I_{dmax}, g_{mmax} values.

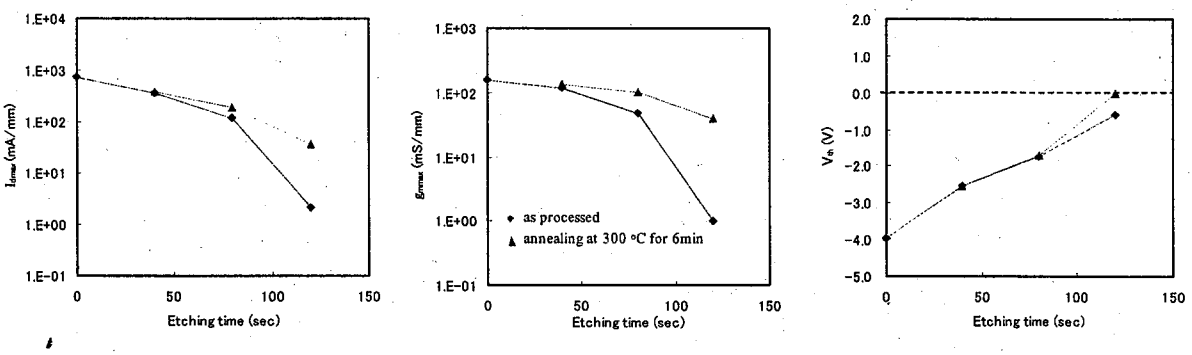

Fig.4.3.2-3 The plot of I_{dmax}, g_{mmax} and V_{th} as a function of gate recess etching time for as-etched and post annealed device (L_g=2μm, W_g=15μm, L_{sd}= 8μm)

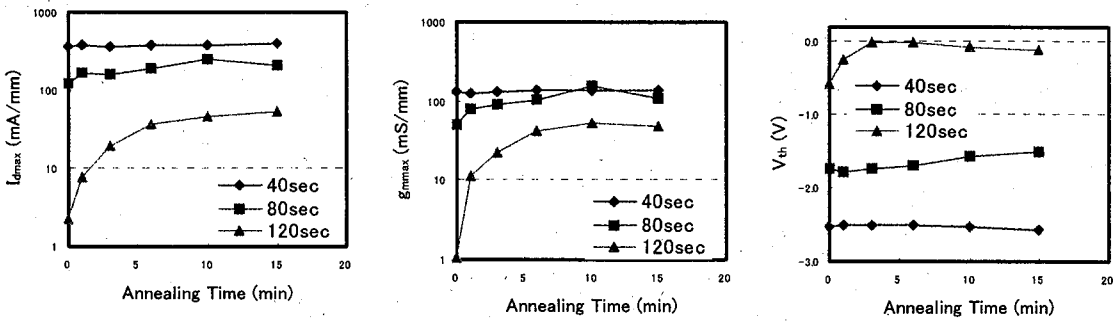

Fig.4.3.2-4 The plot of I_{dmax}, g_{mmax} and V_{th} of gate recessed devices as a function of post annealing time (L_g=2μm, W_g=15μm, L_{sd}= 8μm)

5. Summary

In this report, the growth of AlInGaN and its application for optoelectronic and electronic device were studied. The growth of AlInGaN by MOCVD was optimized as a function of growth temperature. The great difference of material properties were observed between the AlInGaN samples with same composition grown at different temperatures. The material quality of high temperature grown sample is much superior to that of low temperature one. Base on this point, high quality MQWs structure was grown with a strong PL emission at 350 nm. However, the 350nm LED was failed to be fabricated because of lack of a proper AlGaN template on sapphire substrate. The electronic application of AlInGaN was

also studied. Being the key point of HFETs, the Schottky contact was examined first. Finally, both AlInGaN based E-mode and D-mode HFETs were demonstrated for the first time with a high performance, which indicate quaternary AlInGaN is a promising material for high power and high frequency electronic applications.

Acknowledgement:

The Author would like to appreciate Prof. Takashi Egawa, the director of Research Center of Nano-Device and System, for his constant support to this study, for his valuable directing and encouraging; the author is also grateful to Prof. Takashi Jimbo, Associate Prof. Chunlin Shao and Hiroyasu Ishikawa for their help and valuable discussion. Many thanks are also given toDr., Dr. Baijun Zhang, Dr. Hao Jiang, Dr. Maosheng Hao, Dr. Yijun Sun, Dr. Subramaniam Arulkumaran, Dr. S. Lawrence Selvaraj, Dr. Satoru Senta, and the other members of Research Center of Nano-Device and System, for their kind help and enlighten discussion. Appreciations should be also expressed to Japan Society for the Promotion of Science (JSPS), Taiyo Nippon Sanso Corporation and Aichi/Nagoya Knowledge Cluster of Aichi Science and Technology Foundation for their financial support in this study.

Reference

[1]H. Hirayama, J. Appl. Phys., 97, 091101 (2005).

[2]J. Li, K. B. Nam, K. H. Kim, J. Y. Lin, H. X. Jiang, Appl. Phys. Lett. 78, 61 (2001).

[3]H. Hirayama, A. Kinoshita, T. Yamabi, Y. Enomoto, A. Hirata, T. Araki, Y. Nanishi, Y. Aoyagi, Appl. Phys. Lett. 80, 207 (2002) .

[4]X.H. Wu, C.R. Elsass, A. Abare, M. Mach, S. Keller, P.M. Petroff, S.P. DenBaars, J.S. Speck, S.J. Rosner, Appl. Phys. Lett. 72, 692 (1998).

[5]S. Mahanty, M. Hao, T. Sugahara, R.S.Q. Fareed, Y. Morishima, Y. Naoi, T. Wang, S. Sakai, Mater. Lett. 41, 67 (1999).

[6]P.Q. Miraglia, E.A. Preble, A.M. Roskowski, S. Einfeldt, R.F. Davis, J. Crystal Growth 253, 16 (2003).

[7]Y. Liu, T. Egawa, H. Ishikawa and T. Jimbo, J. Crystal Growth, 259, 245 (2003)

[8]Y.-H. Cho, G. H.Gainer, A. J. Fischer, J. J. Song, S. Keller, U. K. Mishra, S.P. Denbaars, Appl. Phys. Lett. 73, 1370 (1998).

[9]H. S. Kim, R. A. Mair, J. Li, J. Y. Lin, and H. X. Jiang, Appl. Phys. Lett. 76, 1252 (2000).

[10]A. Bell, J. Christen, S. Srinivasan, F.A. Ponce, S. Tanaka, H. Omiya, A. Fujioka and Y. Nakagawa, International Conf. on Nitride Semicondcutor (ICNS-5), Nara, Japan, Mo-P1.060, (2003)

[11]C.-H. Chen, L.-Y. Huang, Y.-F. Chen, Appl. Phys. Lett. 80, 1397 (2002).

[12]T. Wang, Y. H. Liu, Y. B. Lee, J. P. Ao, J. Bai, S. Sakai, Appl. Phys. Lett. 81, 2508 (2002).

[13]P.G. Eliseev, P. Perlin, J. Lee, and M. Osinski, Appl. Phys. Lett. 71, 569 (1997).

[14]M. E. Aumer, S. F. LeBoeuf, F. G. McIntosh, S. M. Bedair, Appl. Phys. Lett.75, 3315 (1999).

[15]M. Asif Khan, J. N. Kuznia, R. A. Skongman, D. T. Olson, M. Mac Millan, and W. J. Choyke, Appl. Phys. Lett. 61, 2539 (1992).

[16]K. Joshin, T. Kikkawa, H. Hayahsi, T. Maniwa, S. Yokokawa, M. Yokoyama, N. Adachi, and M. Takikawa, Technical Digest of IEDM, Washington, DC, 8-10 December 2003, P. 983.

[17]O. Ambacher, B. Foutz, J. Smart, J. R. Shealy, N. G. Weimann, K. Chu, M. Murphy, A. J. Sierakowski, W. J. Schaff, L. F. Eastman, R. Dimitrov, A. Mitchell, and M. Stutzmann, J. Appl. Phys. 87, 334 (2000).

[18]M. Asif Khan, J. W. Yang, G. Simin, R. Gaska, M. S. Shur, Hans-Conrad zur Loye, G. Tamulaitis, A. Zukauskas, David J. Smith, D. Chandrasekhar, and R. Bicknell-Tassius, Appl. Phys. Lett. 76, 1161 (2000).

[19]E.T. Yu, X.Z. Dang, P.M. Asbeck, S.S. Lau, and G.J. Sullivan, J. Vac. Sci. Technol. B 17, 1742 (1999).

[20]F. Bernardini, V. Fiorentini, and D. Vanderbilt, Phys. Rev. B 56, R10024 (1997).

[21]S.M.Sze, Physics of Semiconductor Devices, 2nd ed. (Wiley, New York, 1981), pp.245-311.

[22]S. N. Mohammad and H. Morkoc, Prog. Quant. Electron. 20, 361 (1996).

[23]V. W. L. Chin, T. L. Tansley, and T. Osotchan, J. Appl. Phys. 75, 7365 (1994).

[24] J. D. Guo, F.M. Pan, M. S. Feng, R. J. Guo, P.F. Chou, and C. Y. Chang, J. Appl. Phys. 80, 1623 (1996).

[25] J. D. Guo, M. S. Feng, R. J. Guo, F. M. Pan, and C. Y. Chang, Appl. Phys. Lett. 67, 2657 (1995).

[26] E.F. Schubert, Doping in III-V Semiconductors (Cambridge University Press, Cambridge 1993), p.492.

[27]E. H. Rhoderick and R. W. Williams, Metal-Semiconductor Contacts, 2nd edition, Clarendon press, Oxford (1988)

[28]M. W. Wang, J. O. McCaldin, J. F. Swenberg, T. C. McGill, and R. J. Hauenstein, Appl. Phys. Lett. 66, 1974 (1995).

[29]E. Monroy, F. Calle, R. Ranchal, T. Palacios, M. Verdu, F. J. Sanchez, M. T. Montojo, M. Eickhoff, F. Omnes, Z. Bougrioua, and I. Moerman, Semicond. Sci. Technol. 17, L47 (2002).

[30] E. Monroy, F. Calle, J. L. Pau, F. J. Sanchez, E. Munoz, F. Omnes, B. Beaumont, and P. Gibart, J. Appl. Phys. 88, 2081 (2000).

[31]M. Khan, H. Nakayama, T. Detchprohm, K. Hiramatsu, and N. Sawaki, Solid-State Electron. 41, 287 (1997).

[32]L. Zhou, A. T. Ping, K. Boutros, J. Redwing, and I. Adesida, Electron. Lett. 35, 745 (1999).

[33]D. Qiao, L.S. Yu and S. S. Lau, J. M. Redwing, J. Y. Lin, and H. X. Jiang, J. Appl. Phys. 87, 801 (2000).

[34]A. Y. Polyakov, N.B. Smirnov, A.V. Govorkov, D. W. Greve, M. Skowronski, M. Shin, and Joan M. Redwing, MRS Internet J. Nitride Semicond. Res. 3, 37 (1998).

[35] V. Kumar, D. Selvanathan, A. Kuliev, S. Kim, J. Flynn, and I. Adesida, Electron. Lett. 39, 747, (2003).

[36] N. Kubota, J. Ao, D. Kikuta, and Y. Ohno, Jpn. J. Appl. Phys. 43, 4159 (2004).

[37]H.C. Card and E.H. Rhoderick. J. Phys. D4, 1589 (1971).

[38]R.F. Broom, H.P. Meir and W. Walter. J. Appl. Phys. 60, 1833 (1986).

[39]V.L. Rideout and C.R. Crowell, Solid-St. Electron. 13, 993 (1970).

[40]J. H. Werner and H.H. Guttler, J. Appl. Phys. 69, 1522 (1991).

[41]R.T. Tung, Phys. Rev. B, 45, 13509 (1992).

[42] D. K. Schroder, Semiconductor Material and Device Characterization, 2nd edition, p.136, A Wiley-Interscience Publication.

[43]A. Bell1, J. Christen, S. Srinivasan1, C. Plumlee1, H. Omiya1, F.A. Ponce1, S. Tanaka, A. Fujioka, and Y. Nakagawa, J. Appl. Phys. 95, 4670 (2004)

[44] C. M. Jeon, H. W. Jang and J. Lee, Appl. Phys. Lett. 82, 391 (2003).

[45]C. M. Jeon, J. Lee, Appl. Phys. Lett. 95, 698 (2004).

[46]N. Miura, T. Nanjo, M. Suita, T. Oishi, Y. Abe, T. Ozeki, H. Ishikawa, T. Egawa, and T. Jimbo, Solid-St. Electron. 48, 689 (2004).

[47]C. M. Jeon, J. Lee, Appl. Phys. Lett. 82, 4301 (2003).

[48]A. Sozza, C. Dua, E. Morvan, B. Grimbert, M. A. di Forte-Poisson, S. L. Delage and E. Zanoni, Electron. Lett. 41, 927 (2005).

[49]T. Nanjo, N. Miura, T. Oishi, M. Suita, Y. Abe, T. Ozeki, S. Nakatsuka, A. Inoue, T. Ishikawa, Y. Matsuda, H. Ishikawa, T. Egawa, Jpn. J. Appl. Phys. 43, 1295 (2004).

[50] Z. Lin, W. Lu, J. Lee, D. Liu, J. S. Flynn and G. R. Brandes, Appl. Phys. Lett. 82, 4364 (2003)

[51]M. Miyoshi. M. Sakai, H. Ishikawa, T. Egawa, T. Jimbo, M. Tanaka and O. Oda, J. Cryst. Growth 272, 293 (2004).

[52]L. S. Yu, Q. J. Xing, D. Qiao, S. S. Lau, K. S. Boutros, and J. M. Redwing, Appl. Phys. Lett. 73, 3917 (1998).

[53]E. T. Yu, X. Z. Dang, L. S. Yu, D. Qiao, P. M. Asbeck, S. S. Lau, G. J. Sullivan, K. S. Boutros and J. M. Redwing, Appl. Phys. Lett., 73, 1880 (1998).

[54]M. Miyoshi, M. Sakai, S. Arulkumaran, H. Ishikawa, T. Egawa, M. Tanaka and O.Oda: Jpn. J. Appl. Phys. 43, 7939 (2004).

[55]H. Jiang, G. Y. Zhao, H. Ishikawa, T. Egawa, T. Jimbo, and M. Umeno: J. Appl. Phys. 89, 1046 (2001).

[56]W.B. Lanford, T. Tanaka, Y. Otoki and I. Adesida, Electron. Lett. , 41, 449 (2005)

[57]A. Endoh, Y. Yamashita, K. Ikeda, M. Higashiwaki, K. Hikosaka, T. Mastui, S. Hiyamizu and T. Mimura, Jpn. J. Appl. Phys., 43, 2255 (2004)

[58]Y. Cai, Y. Zhou, K. J. Chen, and K.M. Lau, IEEE Electron. Device Lett., 26, 435 (2005).

[59] X, Hu, G. Simin, J. Yang, M. Asif. Khan, R. Gaska, and M.S. Shur, Electron. Lett., 36, 754 (2000).